AIAA JOURNAL

Aeropropulsive Performance Modeling of Over-the-Wing Propulsion at Incidence

Hasse N. J. Dekker* and Marthijn Tuinstra†
Royal Netherlands Aerospace Centre, 8316 PR Marknesse, The Netherlands
and
Woutijn J. Baars,‡ Fulvio Scarano,§ and Daniele Ragni¶
Delft University of Technology, 2629 HS Delft, The Netherlands

https://doi.org/10.2514/1.J064985

A semi-analytical model is proposed that incorporates aerodynamic interactions between the rotor- and wing-induced flowfields. Predictions are validated through experiments performed with an array of five rotors above an airfoil, where the angle of attack, advance ratio, and chordwise rotor position are varied. At moderate angles of attack, the propulsive thrust is reduced due to the acceleration induced by the wing's circulation. Around the stall angle of the isolated wing, the rotors re-energize the boundary layer when operated in low-thrust conditions. By increasing the thrust, a pronounced region of reverse flow between the rotors and wing adversely affects the leading-edge separation delay over the wing that occurs for lower thrust settings. However, in this condition, the wing–rotor-array system exhibits increased thrust compared to the attached flow condition due to the rotors ingesting low-momentum flow. In addition, the rotor-induced flow over the wing augments suction, while the pressure side is subjected to a pressure increase, ascribed to flow entrainment from the rotors. After comparison with the experimental observations, it is confirmed that the model predictions accurately describe the lift and thrust performance trends, aside from a discrepancy in the lift force when the rotors are operated in low-thrust conditions.

Nomenclature

a = induced velocity factor
B = number of blades
C_p = pressure coefficient, $C_p = (p - p_\infty)/q$
C_T = thrust coefficient, $C_T = T/(\rho n^2 D^4)$)
CNC = computer numerical control
c = wing chord, m
c_d = two-dimensional drag coefficient, $c_d = D/(qcS)$
c_l = two-dimensional lift coefficient, $c_l = L/(qcS)$
D = drag force on the wing, N
D_1 = rotor diameter, m
DEHS = di-ethyl-hexyl-sebacat
J = rotor advance ratio, $J = V_\infty/(nD_1)$
J_{eff} = effective rotor advance ratio
J_{T0} = rotor advance ratio for zero thrust conditions
N_r = number of rotors
n = rotor shaft frequency, Hz
p = pressure, Pa
PIV = particle image velocimetry
q = freestream dynamic pressure, Pa
Q = rotor torque, $\mathrm{N \cdot m}$
R_1 = rotor radius, m
Re_c = chord-based Reynolds number
R_s = radius of streamtube, m
r_c = wing's nose radius, m
S = wing span, m
S_D = rotor disk surface, m^2
sCMOS = scientific complementary metal oxide semiconductor
T = rotor thrust, N
V = velocity magnitude, $\mathrm{m \cdot s^{-1}}$
x = x-position from wing's leading edge, m
x' = x-position from the rotor ($x' = x - x_r$), m
x_r = x-position of the rotor tip from wing's leading edge, m
y = y-position from wing's leading edge, m
y_r = y-position of the rotor shaft from wing's surface, m
y_{SL} = shear layer height, m
y_t = rotor tip gap from wing's surface ($y_t = y_r - R_1$), m
α = geometric angle of attack, rad
α_{eff} = effective angle of attack, rad
α_c = stall angle, rad
δ_{99} = boundary-layer thickness, m
$\Delta\alpha$ = difference in effective angle of attack from isolated wing ($\Delta\alpha = \alpha_{\mathrm{eff}} - \alpha_w$), rad
ϵ = streamtube deflection angle, rad
θ = azimuthal coordinate, rad
ρ = density of air, $\mathrm{kg \cdot m^{-3}}$
τ = tracer particle relaxation time, s
Ω = shaft frequency ($\Omega = 2\pi n$), rad/s

Subscripts

e = outlet streamtube condition
t = blade tip condition
w = isolated wing condition
∞ = freestream condition

I. Introduction

RECENT developments in electric propulsion technology have made electric flight over short distances a competitive solution to other means of transportation. The small size, high power-to-weight ratio, and efficiency of electric motors allow for increased design freedom for the propulsion system, extensively enabling

---

Presented as Paper 2023-3355 at the AIAA AVIATION 2023 Forum, San Diego, CA, June 12–16, 2023; received 15 October 2024; accepted for publication 15 May 2025; published online 31 July 2025.

*Ph.D. Candidate, Vertical Flight and Aeroacoustics Department; hasse.dekker@nlr.nl. Member AIAA.

†Head of Department, Vertical Flight and Aeroacoustics Department; marthijn.tuinstra@nlr.nl. Member AIAA.

‡Associate Professor, Aerodynamics, Faculty of Aerospace Engineering; w.j.baars@tudelft.nl. Senior Member AIAA.

§Full Professor, Aerodynamics, Faculty of Aerospace Engineering; f.scarano@tudelft.nl. Member AIAA.

¶Associate Professor, Wind Energy, Faculty of Aerospace Engineering; d.ragni@tudelft.nl. Member AIAA.

distributed propulsion. Consequently, disruptive solutions are currently being developed [1], resulting in unexplored aerodynamic and aeroacoustic installation effects. This trend of moving toward distributed electric propulsion (DEP) with multiple rotors is particularly evident in the upcoming market of electric vertical takeoff and landing vehicles (eVTOLs) [2]. Aircraft designs exist in great diversity and are generally grouped in four categories: multirotors, lift + cruise, tilt-rotors, and tilt-wing vehicles [3,4].

The latter make use of tiltable wings and fixed-pitch (ducted or open) rotors to combine takeoff and landing flexibility with an efficient forward flight. This creates a complex flight envelope, consisting of vertical takeoff, hover, transition, and climb before cruise conditions are reached [5]. During the transition phase, the lift force of the vehicle gradually changes from being generated by propulsive thrust to being generated by the wing's circulation. Consequently, the flight conditions are characterized by low advance ratios and high angles of attack in close proximity to the stall regime [3].

Conceptual tilt-wing vehicles employ an array of propulsors arranged along the wing [1]. A widely used example of this is the leading-edge distributed electric propulsion (LE-DEP) layout, where rotors are installed on pylons aligned with the chord and connected to the wing's leading edge. This rotor orientation increases the wing's lift curve slope, the maximum lift coefficient, and the stall angle [6,7]. An alternative to LE-DEP is to mount propulsors over the suction side of the wing, as schematically illustrated in Fig. 1. This configuration is referred to as over-the-wing distributed electric propulsion (OTW-DEP) and has several adverse and beneficial aerodynamic installation effects. All in all, on the aircraft level, it has shown promise to increase the aeropropulsive efficiency. The study of de Vries et al. [8] revealed an efficiency increase of up to 9%, compared to an isolated propulsion-wing system (although with an uncertainty of ±5%). OTW-DEP configurations are also considered superior in aeroacoustic terms (compared to LE-DEP) because the wing has the potential to shield rotor noise, effectively reducing fly-over noise [9].

When concentrating on the aerodynamics of an OTW-DEP system, the flow is accelerated over the suction side of the wing by both the upstream and downstream parts of the rotors' stream tubes, lowering the static pressure. This has a favorable effect on the aerodynamic efficiency of the system. Müller et al. [10] reported an increase of 8% in the lift-to-drag ratio of an OTW propeller, caused by a lift increase and (pressure) drag reduction. The effect of the propeller tip speed on the aeropropulsive forces was investigated by Perry et al. [11], who noted an increase of the lift force and lift slope, yawing moment, rolling moment, and nose-down pitching moment with increasing propeller tip speed. Furthermore, Marcus et al. [12] revealed that the total lift increase is sensitive to the chordwise position of the propeller. A propeller position closer to the trailing edge provides the largest increase in the wing's lift, caused by the larger area of reduced surface pressure (increased suction) upstream of the propeller. When considering drag, however, others have shown an increase due to the presence of the propeller [13] or have shown that drag is minimized for a propeller positioned in close proximity to where the airfoil attains its maximum thickness [14,15]. Propeller placement is not trivial, given that the resulting static pressure imprint on the wing can result in flow separation. That is, at the location of the propeller, a sharp increase in pressure occurs and can trigger flow separation when the propeller is installed upstream of a region with a strong adverse pressure gradient, e.g., induced by a deflected flap [10,16]. Apart from the aerodynamic effects of the propeller on the wing, the performance of the propeller is also affected by the presence of the wing. The wing circulation induces lower pressure at the rotor disk and nonuniform flow in the wing-normal direction, in turn resulting in unsteady blade loading. As a consequence, propeller efficiency losses up to 16% have been reported, alongside an expected increase in the tonal component of the propeller's noise signature [10].

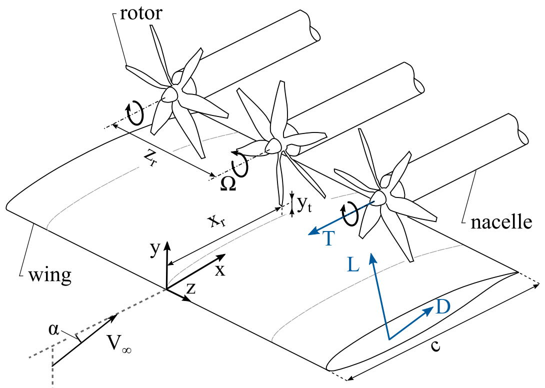

Fig. 1 Schematic representation of over-the-wing propulsion with relevant system parameters and definition of aeropropulsive forces.

Design optimization of OTW propulsion systems requires low-fidelity predictive tools to efficiently vary parameters related to the geometry and aerodynamic performance of the rotor and wing of these systems. Existing low-fidelity tools for integrated propulsion systems [12,14,17–19] typically employ iterative schemes to include the coupling between propulsors and lifting surfaces. Although such methods are computationally efficient, the iteration scheme obscures the impact of the dominant design parameters. Moreover, data-informed guidance of these models is valuable to test their validity, but the majority of previous investigations of OTW propulsors dealt with cruise flight conditions, i.e., the propellers operate at relatively high advance ratios and the system operates at moderate angles of attack. For eVTOL flight, however, lower advance ratios and higher incidence angles are encountered. These higher propulsive thrust conditions are associated with unexpected interactions with surfaces, as shown by Murray et al. [20] for a propeller ingesting a turbulent boundary layer.

1. *Present Contribution and Outline*

In the current study, a semi-analytical model to study and predict aerodynamic interactions of OTW propulsion is formulated, with a focus on the effect of the system's angle of attack and the interpretability of the final expression. The thrust–lift interactions are parameterized as a function of the geometric and operating parameters of the rotor array and wing, and, by employing a single-pass strategy, such design properties appear explicitly in the formulation. Wind tunnel experiments are then conducted to provide insight into the flow topology of OTW propulsion and its interaction with the lifting surface and yield data to validate the model.

The rest of the paper is structured as follows: In Sec. II, the flow hypothesis is introduced and the aeropropulsive model is derived. Section III deals with the experimental setup, and Sec. IV describes the general flow features of the rotor–wing system. Finally, in Sec. V, the model is validated by analyzing performance trends and comparing those to experimental data.

II. Low-Fidelity Model of Over-the-Wing Propulsion

A model is proposed for describing the thrust and lift performance of an over-the-wing propulsion system. Thrust force T is here defined as the integral loading over the rotor disk, acting parallel to the rotor axis. Lift force L is defined as the force perpendicular to the flow direction, generated by the wing only. These two forces are both schematically illustrated in Fig. 1 and are modeled by adopting the superposition principle of the wing and rotor-induced effects. The effect of the rotor induction on the wing's drag is not included in the aeropropulsive model.

The modeling approach itself first considers the wing's influence on the rotor system. A prediction of the rotor-array thrust is obtained by taking the flow pattern over the isolated wing into account, resulting in an effective advance ratio that is combined with the isolated rotor performance trend ($C_{t,\mathrm{iso}}$-J). Secondly, the predicted rotor thrust is used to generate the flow properties inside the rotor array's streamtube. Finally, the influence of the rotor array on the wing's lift force is considered. The lift force is obtained from a formulation that includes the lift of the isolated wing, with, in addition, the changes induced by the rotor-induced flow in proximity to the suction side of the wing. Hence, a low-order model of aeropropulsive forces is obtained by considering a one-way rotor-array–wing interaction. To enhance the interpretability of the formulation, the modeling approach is not advanced using an iterative procedure of rotor–wing interaction effects. A schematic illustration of the model's flow diagram and outline of this section is presented in Fig. 2. Here, the output is the system performance in terms of the installed rotor thrust coefficient (C_T) and wing lift coefficient (c_l). For this, the model requires an advance ratio J and system angle of attack α as well as the geometric parameters of the rotor–wing system. In addition, aerodynamic performance characteristics of the *isolated* wing and rotors are used. The wing's aerodynamic performance comes in through the lift coefficient as a function of the angle of attack, while the isolated rotor's performance comes in through a thrust coefficient as a function of the advance ratio.

A. Wing Effect on Rotor Thrust

When neglecting stall on the rotor blades, which is generally valid for the vehicle's design conditions, the thrust coefficient C_T exhibits a linear dependence on the advance ratio for fixed-pitch rotors. The slope $\mathrm{d}C_T/\mathrm{d}J$ and base $C_{T,h}$ of this relation are specific for each rotor design. Since the thrust of the isolated rotor is often known a priori or can be computed with relative ease, these are defined as performance variables in Eq. (1).

$$C_T = \frac{\mathrm{d}C_T}{\mathrm{d}J} J_{\mathrm{eff}} + C_{T,h} \tag{1}$$

Here, C_T is the thrust coefficient of the installed rotor, and J_{eff} is the effective advance ratio taking into account the wing-induced velocity. Note that, while a linear relation for $C_T(J)$ is used, other functional forms are permitted in case the linear dependency does not apply to the specific rotor geometry and/or operating regime being considered. A modeling strategy is proposed next in order to compute J_{eff}.

1. Advance Ratio Correction

To model the effective advance ratio, the parameterized geometry of Fig. 3a is used. Here, the rotor disk with diameter $D_1 = 2R_1$ is centered at the position of the rotor axis (x_r, y_r). The velocity distribution captured by the rotors can be decomposed into axial and nonaxial components. The former is further split into the uniform (spatial average) and nonuniform (wing proximity) contributions (see Fig. 3b). Since the focus of the current work is to predict the steady (time-averaged) loads of fixed-pitch rotors, only the uniform, axial component of the inflow needs to be considered. The zero-mean nonuniform and the nonaxial inflow components predominantly yield azimuthal variations in blade loading and are primarily relevant to the rotor's far-field acoustics. Note that, for extreme angles of attack and/or high advance ratios, nonaxial inflow could result in elevated steady thrust [21,22]. Such conditions, however, fall outside the investigated parameter space. Additionally, considering that the wing deflects the streamline for OTW propulsion, flow angularity at the rotor is reduced compared to an isolated configuration.

In the model, the wing aerodynamics are split into an inviscid and viscous contribution. The inviscid part accounts for the axial velocity increase by the circulation distribution over the wing's profile. A viscous contribution accounts for leading-edge separation over the wing, occurring at large angles of attack. Other viscous effects, such as the rapid increase in boundary-layer thickness along the adverse pressure gradient region, are disregarded, as this only affects rotors that are installed with minuscule tip gaps, i.e., $y_t < \delta_{99}$ (not considered in the present work).

Contributions from inviscid and viscous flow effects to the isolated rotor's advance ratio J are modeled with two correction factors,

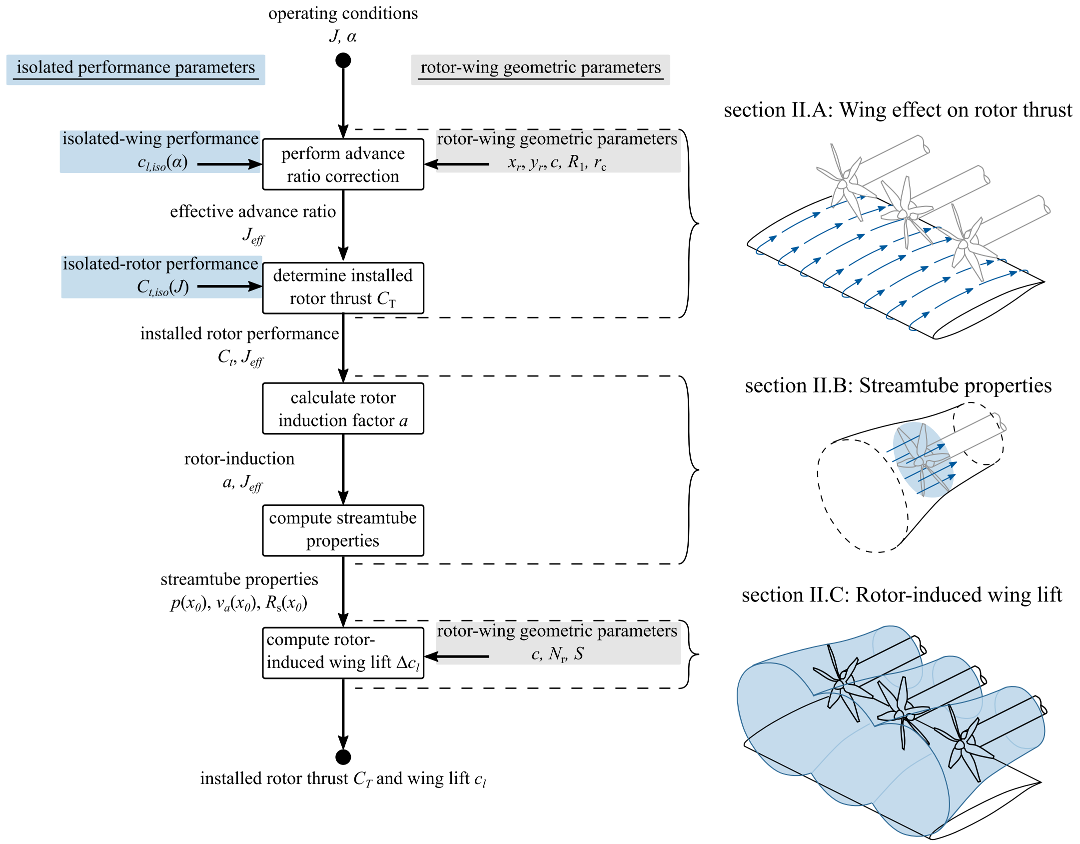

Fig. 2 Flow diagram of the aeropropulsive model.

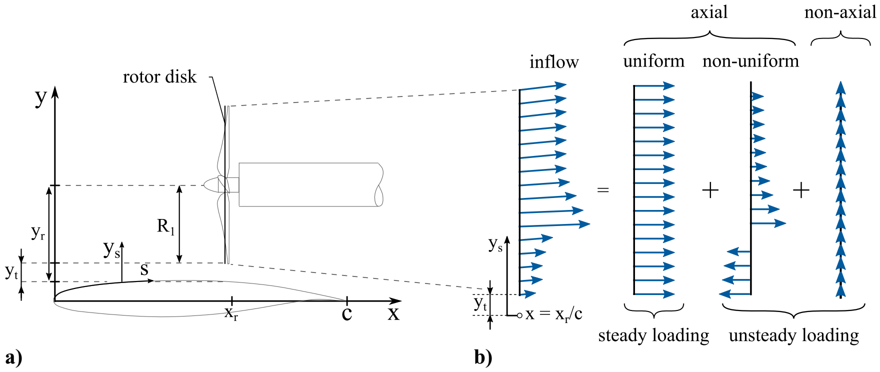

Fig. 3 **a) The 2D system of coordinates and b) decomposition of inflowfield at the disk plane.**

J_Γ and J_{SL}, respectively. This will yield the effective advance ratio, according to

$$J_{\mathrm{eff}} = J \cdot J_\Gamma \cdot J_{\mathrm{SL}} \tag{2}$$

The correction factors J_Γ and J_{SL} are derived as a function of the geometric and performance parameters of the rotor–wing system, with a focus on interpretability and generality of the model. A simplified description is presented in the next sections. For additional details the reader is directed to Appendices A.1 and A.2.

2. *Inviscid: Wing's Circulation*

The axial induced velocity in a reference point $\boldsymbol{r}$ by a set of vortex filaments $\Gamma(s)$ can be found by integration of the Biot–Savart law [23]. The advance ratio correction, by the wing's circulation J_Γ, is then defined as the induced axial velocity, averaged over the rotor disk:

$$J_\Gamma = \frac{V_{\Gamma,x}}{V_\infty} = \underbrace{\frac{1}{\pi R_1^2}\int_A \overbrace{\frac{\hat{\boldsymbol{n}}_{\boldsymbol{x}}}{V_\infty}\int_s \frac{\Gamma(\boldsymbol{s})}{4\pi}\,\frac{\boldsymbol{s}\times\boldsymbol{r}}{|\boldsymbol{r}|^3}\,\mathrm{d}\boldsymbol{s}}^{\text{axial induction by vortex filaments}}\;\mathrm{d}A}_{\text{disk-average}} \tag{3}$$

For an airfoil, the bound vortex filaments typically lie along its contour, making the integration of Eq. (3) rather cumbersome. The problem is modeled by making use of thin airfoil theory, with a parabolic distribution of vortex filaments $\Gamma(x)$ along the chord line, as schematically illustrated in Fig. 4a. The strength of the vorticity source $\Gamma(x)$ depends on the lift coefficient of the wing:

$$\Gamma(x) = \frac{3}{4}c_l V_\infty c\left(1-\frac{x^2}{c^2}\right) \tag{4}$$

A second simplification is made by extracting the axial induction only at the center point of the rotor disk, i.e., the rotor axis (x_r, y_r), which corresponds with sufficient accuracy to the disk-averaged value (relative error below 1%). The simplified expression for J_Γ becomes

$$J_\Gamma \approx \frac{1}{2\pi V_\infty}\int_0^c \frac{\Gamma(x)y_r}{(x_r-x)^2+y_r^2}\,\mathrm{d}x \tag{5}$$

which can be integrated analytically.

3. *Viscous: Shear Layer Ingestion*

Wing stall is implemented by considering that flow separation occurs abruptly at the leading edge when the angle of attack exceeds a given stall angle α_c. Consequently, the advance ratio needs to be corrected to account for the fraction of the rotor's area affected by separated flow ingestion, A_{SL}:

$$J_{\mathrm{SL}} = 1 - f(\alpha,\alpha_c)\overbrace{\left(1-\frac{V_{\mathrm{SL}}}{V_\infty}\right)}^{\text{momentum deficit}}\overbrace{\frac{A_{\mathrm{SL}}}{\pi R_1^2}}^{\text{ratio of ingestion}}, \quad f(\alpha,\alpha_c) = \begin{cases} 0, & \alpha < \alpha_c \\ 1, & \alpha \ge \alpha_c \end{cases} \tag{6}$$

In the equation above $f(\alpha,\alpha_c)$ is a stall criterion and V_{SL} is the local velocity in the separated region. A_{SL} is modeled assuming a spanwise homogeneous shear layer, oriented tangential to the freestream direction (see Fig. 4b). Experimental data (later presented in Fig. 13) showed that the shear layer height at the position of the rotor was underpredicted. Therefore, the modeled shear layer profile was adjusted by applying a steeper slope, with a factor of (11/8) compared to the freestream.

The area A_{SL} is obtained by integration (Eq. (7)) and schematically illustrated in Fig. 4c.

$$A_{\mathrm{SL}} = \int_{y_r-R_1}^{y_{\mathrm{SL}}}\sqrt{(y-y_r)^2+R_1^2}\,\mathrm{d}y \tag{7}$$

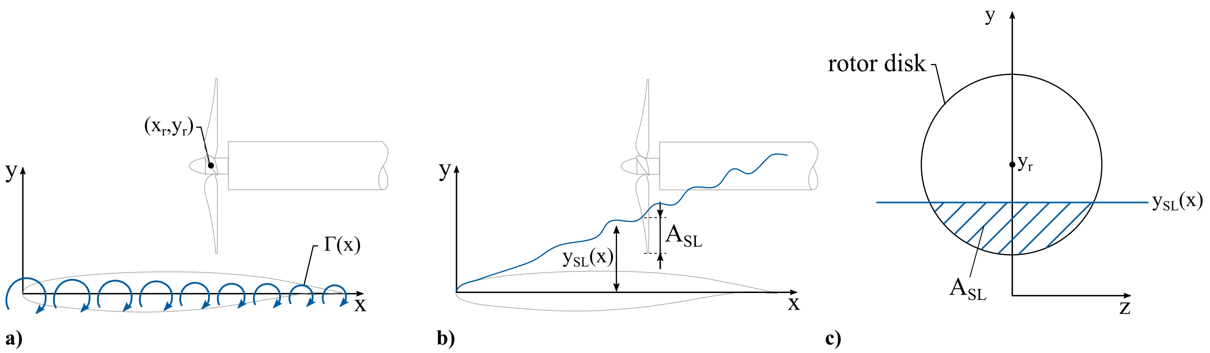

Fig. 4 **Schematic of the modeling strategies for the effective advance ratio: a) the (inviscid) velocity increase by the circulation distribution $\Gamma(x)$ and b) the (viscous) boundary-layer separation at large angles of attack and c) defining the ratio of boundary-layer ingestion.**

To complete the model, the stall angle α_c is found by using an empirical relation as a function of the wing's nose radius to chord length r_c/c [24].

It is worth noting that the model exhibits abrupt separation at the leading edge, differing from the gradual progression of separation from trailing to leading edge, as observed for an isolated wing as the angle of attack increases. Experimental results (later presented in Fig. 10) revealed that, for over-the-wing propulsion, separation occurs more abruptly due to the formation of a flow reversal region between the rotor and wing, indicating that the model accurately captures the observed separation mechanism of the installed system.

B. Streamtube Properties

For modeling the wing's lift force, the influence of the rotor-induced flowfield must be taken into account. Using the actuator disk model, the rotor's induction factor a, defined as the induced velocity v_a normalized by the freestream velocity, can be written as a function of the local advance ratio J_{eff} and the installed rotor's thrust coefficient C_T:

$$a = \frac{v_a}{V_\infty} = \frac{(J_\Gamma \cdot J_{\mathrm{SL}})}{2}\left(\sqrt{\frac{8C_T R_1^2}{S_D J_{\mathrm{eff}}^2} + 1} - 1\right) \tag{8}$$

Following a similar approach as in the work of Veldhuis [14], the rotors can be modeled by a uniform distribution of doublets of strength Δp over the disk surfaces (as shown in Fig. 5a). Considering that a spanwise distributed array of rotors is used in the current work, the doublets are instead redistributed on a rectangular surface with height $\mathrm{d}y = 2R_1$ and width $\mathrm{d}z = 2N_r R_1$ (here N_r is the number of rotors considered; see Fig. 5b).

It can then be shown (see Sec. B.1 for a detailed derivation) that for rotor numbers of $N_r \geq 5$, the streamwise distribution of streamtube quantities approaches the two-dimensional solution ($N_r = \infty$):

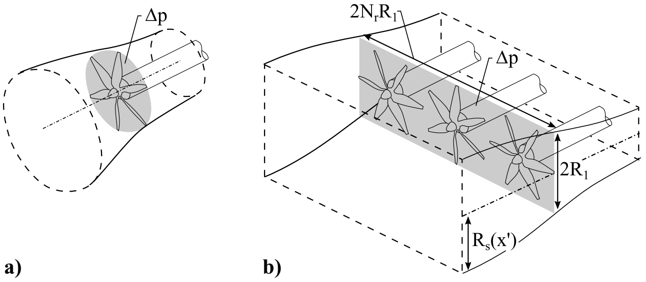

a) b)

Fig. 5 Schematic of the projected pressure doublets with strength Δp on a) a single rotor disk and b) a rectangular disk surface as considered in the aeropropulsive model.

$$\begin{aligned} p(x') &= \frac{\Delta p}{\pi}\tan^{-1}\left(\frac{R_1}{x'}\right) \\ \frac{v_a(x')}{V_\infty} &= a\left(\frac{x'}{\sqrt{x'^2}} + 1 - \frac{2}{\pi}\tan^{-1}\left(\frac{R_1}{x'}\right)\right) \\ \frac{R_s(x')}{R_1} &= \frac{1+a}{1 + a\left(\frac{x'}{\sqrt{x'^2}} + 1 - \frac{2}{\pi}\tan^{-1}\left(\frac{R_1}{x'}\right)\right)} \end{aligned} \tag{9}$$

in which x' denotes the streamwise distance from the rotor's disks, i.e., $x' = x - x_r$. The relations of Eq. (9) are used to predict the lift increase by rotor induction, as is introduced in the next section.

C. Rotor-Induced Wing Lift

Three separate rotor-induced aerodynamic effects on the lift-generating mechanism of the wing are considered in the model (illustrated in Fig. 6). Firstly, a contraction of the rotor's streamtube causes an effective upwash near the wing's leading edge, leading to a lift enhancement $\Delta c_{l,\alpha}$. Secondly, inside the streamtube, the pressure varies compared to the surroundings. This pressure is projected on the wing surface, resulting in $\Delta c_{l,p}$ (see Fig. 6b). Finally, if the wing has camber, this causes the streamtube to deflect downward, creating an additional lift component $\Delta c_{l,tv}$, as shown in Fig. 6c.

The lift increase compared to the isolated wing is modeled by superimposing each of the three rotor-induced flow effects:

$$\Delta c_l = \Delta c_{l,\alpha} + \Delta c_{l,p} + \Delta c_{l,tv} \tag{10}$$

A simplified derivation of the aeropropulsive model is now presented in the next sections; for additional details, the reader is referred to Appendices B.2, B.3, and B.4.

1. *Effective Angle of Attack*

The axial velocity increase v_a in the rotors' streamtubes results in a vertical induced velocity v_i (see Fig. 6a). This generates an effective upwash at the wing's leading edge, resulting in an increase in lift by $\Delta c_{l,\alpha}$. The increase of angle of attack $\Delta\alpha$ by the rotor-induced flow is modeled by the resulting angle between the inflow vectors of the installed configuration and the geometric angle of attack, and by considering the affected span of the wing:

$$\begin{gathered} \Delta c_{l,\alpha} = \overbrace{2\pi}^{\substack{\text{lift}\\ \text{slope}}}\ \overbrace{\Delta\alpha}^{\substack{\text{increase}\\ \text{angle of}\\ \text{attack}}}\ \overbrace{\frac{2N_r R_1}{S}}^{\substack{\text{affected}\\ \text{span}}} = 2\pi\cos^{-1}\left(\frac{\boldsymbol{a}\cdot\boldsymbol{b}}{|\boldsymbol{a}||\boldsymbol{b}|}\right)\frac{2N_r R_1}{S}, \\ \boldsymbol{a} = \begin{bmatrix} \dfrac{v_a(-x_r)}{V_\infty} + \cos(\alpha) \\ \dfrac{v_i(-x_r)}{V_\infty} + \sin(\alpha) \end{bmatrix}, \quad \boldsymbol{b} = \begin{bmatrix} \cos(\alpha) \\ \sin(\alpha) \end{bmatrix} \end{gathered} \tag{11}$$

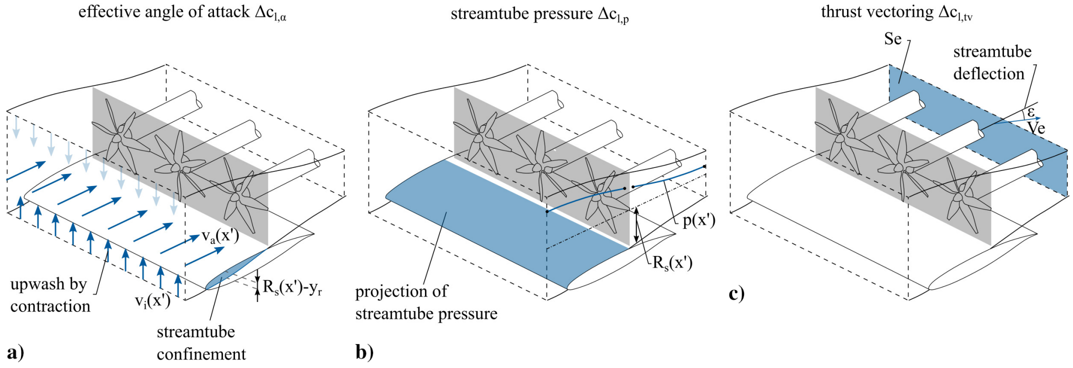

a) b) c)

Fig. 6 Schematic of interactions of the rotors' two-dimensional streamtube on wing's lift: a) upwash by streamtube contraction, b) the streamtube pressure, and c) the streamtube deflection.

in which $\boldsymbol{a}$ is the two-dimensional normalized inflow vector of the installed configuration and $\boldsymbol{b}$ of the isolated wing. The vertical induced v_i follows from v_a (Eq. (9)) by the conservation of mass:

$$\frac{v_i(x')}{V_\infty} = C_1 \frac{\mathrm{d}\frac{v_a(x')}{V_\infty}}{\mathrm{d}x'} R_1 \tag{12}$$

Here, C_1 is a correction factor used to account for the confined streamtube by the presence of the wing. The confinement leads to a higher-than-predicted axial velocity in the streamtube, further reducing the static pressure around the leading edge of the wing and increasing vertical-induced velocity v_i. The correction for this is formulated as a power function of the overlap between the predicted rotors' free-contraction at the position of the leading edge (i.e., $R_s(-x_r)$) and the wing's surface height y_r (see Fig. 7 for the definition of variables), normalized by the rotor radius:

$$\begin{aligned} C_1 &= \max\left(1, c_0\left(\frac{R_s(-x_r) - y_r}{R_1}\right)^{c_1} + 1\right) \\ &= \max\left(1, 60\left(\frac{R_s(-x_r) - y_r}{R_1}\right)^{5/2} + 1\right) \end{aligned} \tag{13}$$

The coefficients c_0 and c_1 are obtained by fitting the experimental results of the effective angle of attack. The experimental results of the effective angle of attack are presented in Sec. V.A, and the details of the fitting process are described in Sec. B.2. Even though the coefficients c_0 and c_1 are based on experimental data, the relation of Eq. (13) is universally applicable to over-the-wing propulsion systems. Nonetheless, to ensure consistency, the coefficients should be tuned through a more comprehensive training database that includes variations in vertical rotor positioning.

2. *Streamtube Pressure*

The rotors' suction leads to a reduction in pressure in front of the disk, while the pressure is increased downstream. The generated lift coefficient $\Delta c_{l,p}$ due to this effect is predicted by integrating the pressure in the streamwise direction:

$$\begin{aligned} \Delta c_{l,p} &= \overbrace{\frac{2N_r R_1}{S}}^{\text{affected span}} \overbrace{\frac{2}{\rho V_\infty^2 c}}^{\text{lift normalization}} \int_{-x_r}^{c-x_r} p^*(x')\,\mathrm{d}x', \\ \text{for } & \frac{\lim_{x' \to -\infty} R_s(x')}{y_r} = \frac{R_1(a+1)}{y_r} > 1 \end{aligned} \tag{14}$$

in which $p^*(x')$ is the projected streamtube pressure over the wing surface (see Fig. 7) for the range of integration. Equation (9) therefore only holds when the pressure is overlapping with the wing surface, explaining the criterion on the right-hand side where the limit function highlights the maximum streamtube radius, also illustrated in Fig. 7. The pressure $p^*(x')$ is based on the relation for the free streamtube pressure $p(x')$, recall Eq. (9), and in addition includes a correction $g(x', y_r)$ that accounts for the reduced pressure due to the streamtube confinement, using Bernoulli's principle:

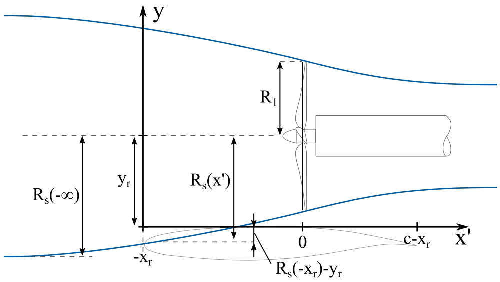

Fig. 7 Schematic of the overlap between the streamtube and wing surface, and the definition of the variables to compute $\Delta c_{l,\alpha}$ and $\Delta c_{l,p}$.

$$\begin{aligned} p^*(x') &= p(x') - \overbrace{\frac{\rho}{2}(v_a(x') + V_\infty)^2 (1 - (g(x', y_r))^2)}^{\text{effect of streamtube confinement}}, \\ g(x', y_r) &= \frac{R_s(x')}{y_r} \end{aligned} \tag{15}$$

Considering that $\Delta c_{l,p}$ is based on the overlap between streamtube height and wing contour, only the upstream region in the integral of Eq. (14) is considered in the aeropropulsive model. Modeling of the lift reduction by the pressure increase downstream of the rotor array relies on the streamtube–wing attachment point, which is determined by complex viscous interactions [16]. Moreover, since the attachment point is moved further downstream for rotors in high-thrust conditions, the effect of the projected pressure is expected to be dominated by the upstream contribution.

For the second term in Eq. (15), the averaged values (in the upstream direction) of the induced velocity v_a and streamtube height R_s are considered. This reduces the complexity of the integral of Eq. (14). Details of the derivation and the final expression for $\Delta c_{l,p}$ are described in Sec. B.3.

3. *Thrust Vectoring*

The third aerodynamic effect is the deflection of the streamtube in the vertical direction, providing a form of thrust vectoring. The lift increase by slipstream deflection $\Delta c_{l,tv}$ follows from a momentum balance using a streamtube deflection angle ϵ, and the velocity V_e and area S_e at the exit of the streamtube (see Fig. 6):

$$\Delta c_{l,tv} = \frac{2S_e(V_e - V_\infty)^2 \epsilon}{V_\infty^2 c}, \qquad \epsilon = \epsilon_w \overbrace{\left(1 - \frac{x_r}{c}\right)}^{\text{rotor position}} = \frac{2c_{l,0}c}{\pi S}\left(1 - \frac{x_r}{c}\right) \tag{16}$$

The deflection angle ϵ is set to be equal to the one of the isolated wing under $\alpha = 0°$, i.e., ϵ_w, with a weighting (as a function of rotor position) to account for effectiveness as a thrust vectoring device. Note that V_e and S_e in Eq. (16) indicate the streamtube velocity and cross-sectional surface in the downstream extend and can be found by taking the limit of Eq. (9) to $x' \to +\infty$.

D. Applicability Range of the Aeropropulsive Model

Several assumptions are made in the derivation of the aeropropulsive model, confining the parameter space over which the method is applicable. An overview of this parameter space, consisting of both geometrical and performance conditions, is provided in Table 1. The origin of the limitation is included in the third column here. Note that the lift part of the model has a more confined applicability range.

Furthermore, any (steady) aerodynamic rotor-to-rotor effects are not included, and the lift model is only applicable when the flow at the leading edge of the wing is attached.

Recall that the calculation of $\Delta c_{l,\alpha}$ includes a correction for streamtube confinement. Excluding this correction affects the predicted lift for aft-mounted rotors at low advance ratios, resulting in a reduction exceeding 15% within the examined parameter space. On a related note, the interactions between the rotor and wing induction are modeled using a single-pass approach, without requiring additional iterations of the aeropropulsive model. An analysis, presented in Appendix C, showed that additional iterations lead to a minor reduction (up to 5%) in the aeropropulsive forces. This minor increase in accuracy therefore does not justify the additional complexity and obscurity of repetitive computations.

III. Experimental Validation

A. Setup and Wind Tunnel

The experiments were performed in the Aeroacoustic Wind Tunnel (NLR-AWT) facility at the Royal Netherlands Aerospace Centre (see Fig. 8). To ensure high quality of the aerodynamic

Table 1 Parameter space of the aeropropulsive performance model

Parameter	Value	Origin
Freestream Reynolds number Re_c	$>250{,}000$	Laminar separation not included in model
Freestream Mach number M	<0.3	Incompressible flow assumed for Eqs. (9) and (15)
Advance ratio J	$0 < J \leq J_{T0}$	Hover and negative thrust conditions are not applicable in Eq. (9).
Rotor chordwise position x_r/c	$0.1 \leq x_r/c \leq 0.9$	Eq. (5) fails to predict wing-induced velocities at leading- and trailing edge
Rotor tip gap y_t	$>\delta_{99}$	Boundary-layer ingestion not included
Rotor spacing z_r/R_1	<1.5 (lift)	Required for 2D-streamtube formulation of Eq. (9)
Number of rotors N_r	≥ 5 (lift)	


a) b)

Fig. 8 a) Exterior of the 0.95 by 0.95 m^2 test section of the NLR-AWT (left) and b) rotor-array–wing setup in the test section (right).

measurements, a closed (0.95×0.95 m^2) test section was used, allowing a freestream turbulence intensity level of 0.01% at a freestream velocity of 20 m/s.

A DLR-F15 wing model was mounted vertically on a turntable in the floor of the closed test section, as shown on the right-hand side of Fig. 8. The wing's chord was 240 mm, and the boundary layer was tripped at 10% chord on both the suction and pressure sides. Over the suction side of the wing, an aerodynamically profiled strut was connected to the same turntable as the wing. The strut serves as a support structure for five spanwise-distributed nacelles and aligns each nacelle's axis to the wing's chord direction. Inside each nacelle, a brushless in-runner motor was used to drive a custom-designed six-bladed rotor (radius of 63.5 mm) at a shaft frequency of 383 Hz in a counter-rotating orientation (the center rotor anticlockwise when looking downstream, illustrated in Fig. 1, and subsequent rotors in alternating directions). The tip-to-tip separation distance between subsequent rotors is $0.05R_1$. The blade design of the rotor is based on a benchmarked version for low-Reynolds-number applications derived from a NACA4412 airfoil. For additional details on the blade design, the reader is directed to the work of Grande et al. [25]. The rotor has been manufactured with CNC out of aluminum with 0.02 mm precision and cured to avoid material relaxation and oxidation. The experimental conditions are summarized in Table 2.

B. Measurement Equipment

Integral loading, surface static pressure, and PIV flow measurement techniques are employed, which are discussed in more detail below. A schematic overview of the measurement system is provided in Fig. 9a. All measurements (with the exception of PIV) were obtained at an acquisition rate of 4096 Hz and averaged over a time frame of 20 s.

1. Integral Loading

Rotor thrust and torque were measured on the center rotor. Its brushless motor was mounted to the nacelle using two parallel-mounted uni-axial FUTEK LSB205 load cells (rated output (RO) of 22.2 N with hysteresis of ±0.1% RO and nonlinearity of ±0.1% RO) and a FUTEK QTA141 torque cell (RO of 1 N · m with hysteresis of 0.5% and nonlinearity of 0.2%; see Fig. 9b). The load and torque cells were excited with 7 volts of direct current (VDC) by a single power supply. Repeated measurements for thrust showed an average deviation of 4%.

The loads of the wing were measured by a custom-made six-component force balance in the floor of the wind tunnel (see Fig. 9a). In the x- and y-directions, the balance has a capacity of 325 and 1800 N, respectively. The uncertainty as a percentage of the full load range is 0.80% for the x-direction and 0.13% for the y-direction.

Table 2 Over-The-Wing rotor system operating conditions

Wing chord c, mm	240
Aspect ratio $Æ$	4
Shaft frequency (Hz)	383
Number of blades B	6
Rotor radius R_1 (mm)	63.5
Rotor tip gap y_t/R_1	0.27
Rotor separation z_r/R_1	2.05
Rotor chord position x_r/c	[0.3, 0.6, 0.9]
Advance ratio J	[0, 0.3, 0.45, 0.6]
Angle of attack α	[−3, 0[a], 2, 4[a], 6, 8[a], 10[a], 11[a], 12[a], 13[a], 14[a], 15, 16, 20[a]]
Wing chord Reynolds number Re_c	240,000–480,000
(3/4) R_1 rotor blade chord Reynolds number Re_b	≈60,000

[a] PIV fields were acquired for these angles of attack, for each rotor position and advance ratio.

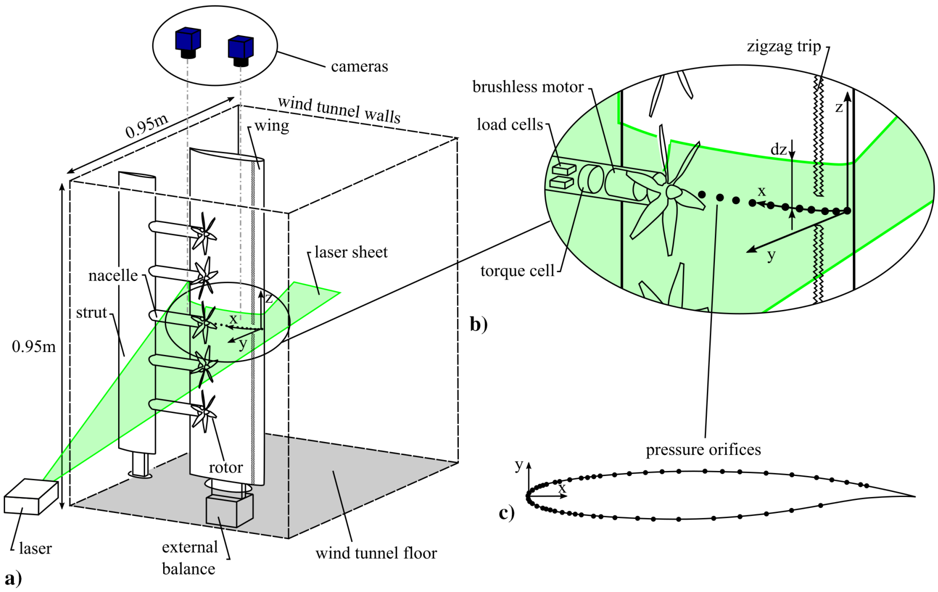

Fig. 9 a) The 3D schematic of the experimental apparatus and coordinate system, b) zoomed-in plot of the measurement techniques around the center rotor, and c) contour of the F15 wing model with location of the static pressure taps.

2. *Pressure Orifices*

The wing's pressure distribution was measured by 59 static pressure taps, located at the center-span of the wing, below the center rotor. The location of the pressure taps along with the contour of the wing profile is presented in Fig. 9c. The pressures were sampled by a Scanivalve ERAD4000 measurement system with a full range of approximately 100 kPa. Based on the spread in the data of repeated measurements, the experimental uncertainty of the static pressures was found to be $\pm 0.0125 C_p$.

3. *Particle Image Velocimetry*

The flow over the suction side of the wing is characterized using planar, 2-Dimensional 2-Component particle image velocimetry (PIV). For this, the flow was seeded with DEHS tracer particles (comprising a relaxation time of $\tau = 2$ μs) that were illuminated by an Evergreen laser (200 mJ/pulse) in a sheet of 3 mm thickness (see Fig. 9a). Illumination was performed at a rate of 15 Hz, and the duration of each pulse (pulse width) was $\delta t = 25$ ns. The center of the laser sheet was positioned with an offset dz in the spanwise direction (see Fig. 9b) of 12 mm from the center rotor axis to avoid any shadows from the nacelle. Particle images were acquired using two sCMOS cameras (Imager sCMOS CLHS), placed outside the wind tunnel test section at a distance of 0.8 m from the measurement region. The cameras were equipped with a lens system of focal length $f = 50$ mm, set at a numerical aperture of $f_\# = 8$. The resulting field of view spans 36×24 cm^2 ($6R \times 4R$). System synchronization was obtained with a LaVision Programmable timing unit (PTU X), and each measurement was composed of at least 200 recordings for a time duration of 13 s. An overview of the illumination and imaging conditions is presented in Table 3.

Planar velocity components were inferred from cross-correlation of two recordings, with a window size of 32×32 px^2 and an overlap of 75%. This resulted in a vector resolution of 2.4 mm and a vector spacing of 1.15 mm. The measurement uncertainty for the time-averaged velocity field is determined by the ratio between the relevant velocity fluctuations (magnitude of the standard deviations) and the square root of the number of statistically independent measurements. This results in an uncertainty of 0.01% of the free-stream velocity in the majority of the domain but locally increases to 6% in shear regions of the flow.

Table 3 2-Dimensional 2-Component PIV illumination and imaging conditions

Seeding type	DEHS
Particle relaxation time, τ (μs)	2
Illumination	Evergreen (200 mJ/pulse)
Sheet thickness, δz (mm)	3
Pulse width, δt (ns)	25
Repetition rate (Hz)	15
Camera type	2 x Imager sCMOS CLHS
Camera resolution	2560×2160 px^2
Objective focal length, f (mm)	50
Numerical aperture, $f_\#$	8
Optical magnification, M	0.07
Field of view (cm^2)	36×24
Number of recordings	200
Image analysis	Cross-correlation (32×32 px^2, 75% overlap)
Vector pitch (mm)	1.15

IV. Results

A. Flowfield Statistics

The general flow features of the rotor–wing system are investigated by considering three levels of inclination for a fixed rotor position of $x_r/c = 0.6$, namely zero angle of attack, an angle of attack of 8°, which positions the rotor in a strong adverse pressure gradient, and the early onset of stall at $\alpha = 12°$. The time-averaged velocity magnitude contours and two-dimensional velocity streamlines in the plane with an offset of $0.2R_1$ in the spanwise direction from the center rotor's axis is presented in Fig. 10. The top row presents results with the rotors removed. Evidently, the acceleration of the flow over the wing's suction side is relatively moderate for $\alpha = 0°$, but increases for $\alpha = 8°$ due to the enhanced circulation of the wing. Inclination of the wing to $\alpha = 12°$, in Fig. 10c, shows that the boundary layer separates close to the leading edge, which marks the onset of stall.

When proceeding to the case of a low thrust condition ($J = 0.6$), an increase of velocity appears over the wing (see Figs. 10d and 10e). The flow is primarily accelerated downstream of the disk, leaving the upstream region largely unaltered. Nonetheless, for $\alpha = 8°$, the induced flow of the rotors causes separation from the wing at roughly $0.8c$ chord (compare Figs. 10b and 10e) by the entrainment of flow toward the slipstream. The result for the early stall condition in Fig. 10f shows that the limited suction of the rotors prevents the boundary layer from reattaching. By reducing the advance ratio to $J = 0.3$, the rotors' thrust increases, leading to a stronger contraction of the rotor's streamtube and higher induced velocities, both upstream and downstream of the disks. The flow

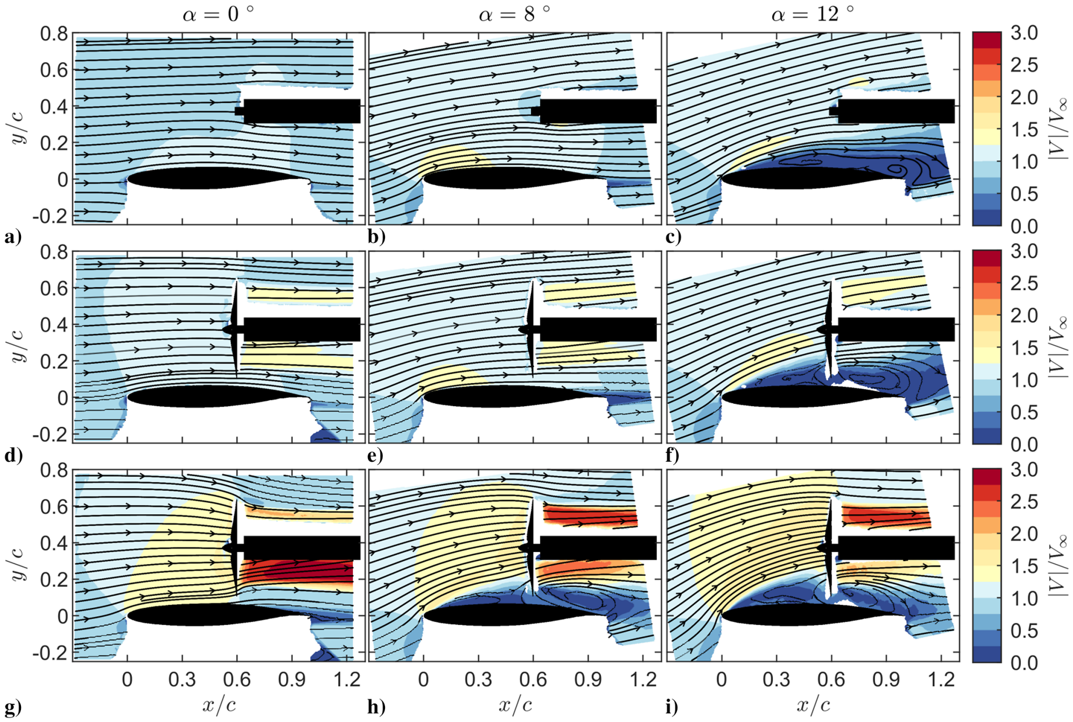

Fig. 10 Normalized velocity magnitude contours and 2D streamlines for $\alpha = 0°$, $\alpha = 8°$, and $\alpha = 12°$ for the rotors-off case (a–c), $J = 0.6$ (d–f), and $J = 0.3$ (g–i). The rotor position is fixed at $x_r/c = 0.6$.

topology, relative to the lower thrust conditions of $J = 0.6$, changes significantly when changing the system's angle of attack. For $\alpha = 8°$ in Fig. 10h, the pressure jump over the rotor disk increases the adverse pressure gradient imposed by the wing and causes the flow to separate. As a consequence, the rotor ingests flow from downstream of the disk, leading to stagnation upstream of the disk. By a combination of this stagnation and the contraction of the slipstream, the flow over the wing separates close to the leading edge. This phenomenon remains unchanged with a further increase in the geometric angle of attack, since the data for $\alpha = 12°$ presents a similar flow topology (see Fig. 10i). However, in this case, the shear-layer height in the upstream region of the rotors has grown by the larger geometric angle of attack.

Another characteristic of the flow that manifests itself strongly for the $J = 0.3$ case is an increase in flow angle upstream of the wing ($x < 0$ and $y < 0$) with respect to the rotors-off conditions (compare Figs. 10a–10c to Figs. 10g–10i). This behavior was included in the aeropropulsive model and will be discussed in more detail in Sec. V.A.

The effect of the rotors on the wing's pressure distribution is shown by the results of the static pressure measurements in Fig. 11. Note that in this case the pressures are extracted directly below the center rotor axis at the wing's surface, without the offset in the spanwise direction as used to generate Fig. 10.

For $\alpha = 0°$ in Fig. 11a, the rotors-off data have comparable pressure distributions on the suction and pressure sides. When including the rotors, the flow accelerates, leading to a lower static pressure upstream of the disk. Downstream of the disks, the total pressure increases, leading to an increase in static pressure on the wing. These effects are noticeable for $J = 0.3$ in particular. The occurrence of a suction peak for $J = 0.3$ and the increase in pressure on the pressure side are effects that are consistent with the observed increase in flow angle, as was observed in Figs. 10g–10i.

Similarly, the pressure profiles for $\alpha = 8°$, presented in Fig. 11b, show an increase of the suction peak up to $C_p \approx -3$ and a stagnation point on the pressure side that moves toward the trailing edge by the rotor-induced flow. However, in the vicinity of the rotor, i.e., $x_r/c = 0.6$, the results are different than those for $\alpha = 0°$. That is, for the inclined system at an advance ratio of $J = 0.3$, a small pressure plateau at $x_r/c = 0.5$ hints upon the occurrence of flow separation. The pressure jump just downstream at the rotor disk location is now reduced in magnitude (Fig. 11a) and is ascribed to the recirculation bubble downstream of the disk, as seen in Fig. 10h.

Finally, in the separated flow region that occurs at $\alpha = 12°$ (see in Fig. 11c), the pressure plateau is visible at $x/c = 0.1$, for the rotors-off condition. For the installed configuration, the

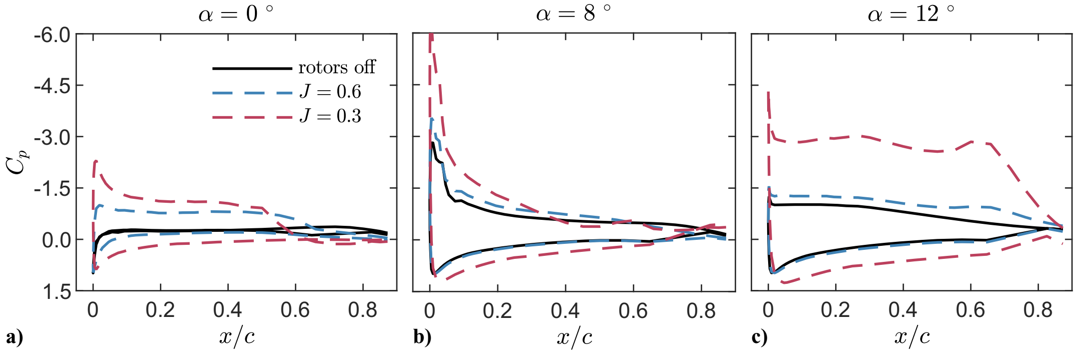

Fig. 11 Pressure coefficient C_p along the wing's contour for the rotors-off condition, $J = 0.6$ and $J = 0.3$: a) $\alpha = 0°$, b) $\alpha = 8°$, and c) $\alpha = 12°$. The rotor position is fixed at $x_r/c = 0.6$.

pressure plateau starts at the same chordwise position, but the pressure is reduced depending on the advance ratio and therefore the rotors' thrust delivered. Note that even though the separation point at the wing is maintained, the effective angle of attack is enhanced, and therefore the flow curvature increases with respect to the rotors-off condition. Additionally, the rotors' suction also deflects the shear layer, which further increases the flow curvature after separation has occurred. As a consequence of these effects, the difference between the installed and rotors-off pressure distribution is more substantial for this angle of attack, and therefore the largest increase in lift is expected in poststall conditions.

B. Boundary-Layer Separation

In the previous section, it was shown that the rotors operating in low thrust conditions ($J = 0.6$) were not able to delay the boundary-layer separation from the wing's leading edge. In addition, for high-thrust conditions, the rotors caused a region of flow reversal between the rotor and wing, leading to local flow separation upstream. These effects are described in more detail now by evaluating boundary-layer profiles along the wing's chord for a relatively fine discretization of the angle of attack.

Figure 12 presents the axial velocity profiles, extracted at different chordwise positions along the wing. For $\alpha = 4°$ (Fig. 12a), the decrease in J causes an increase in axial velocity while maintaining the same profile shape as the rotors-off condition. This persists until $x/c \approx 0.5$, where the axial velocity close to the wing is reduced due to the pressure jump that occurs over the rotor disk for $J = 0.3$. Thereupon, separation downstream of the rotor for this advance ratio is also observed. When the system is inclined to $\alpha = 8°$ in Fig. 12b, the rotor-induced separation is moved further upstream and occurs from $x/c \approx 0.3$ onward. Further inclination, in Figs. 12c and 12d, has no further effect on the flow topology of the data corresponding to $J = 0.3$. In contrast, when the rotors produce limited thrust ($J = 0.6$), they are able to delay flow separation over the wing. Around the isolated wing stall angle of $\alpha = 10°$ (Fig. 12c), the boundary layer remains thinner than the rotors-off condition. This reduction in separation is noticeable both upstream and downstream of the rotor array. This delay in separation disappears again for larger angles of attack, as shown for $\alpha = 11°$ in Fig. 12d.

The effect of the rotors on the location of the separation point and the shear layer profile during ingestion is shown by the distribution of the normalized shear layer height, as presented in Fig. 13.

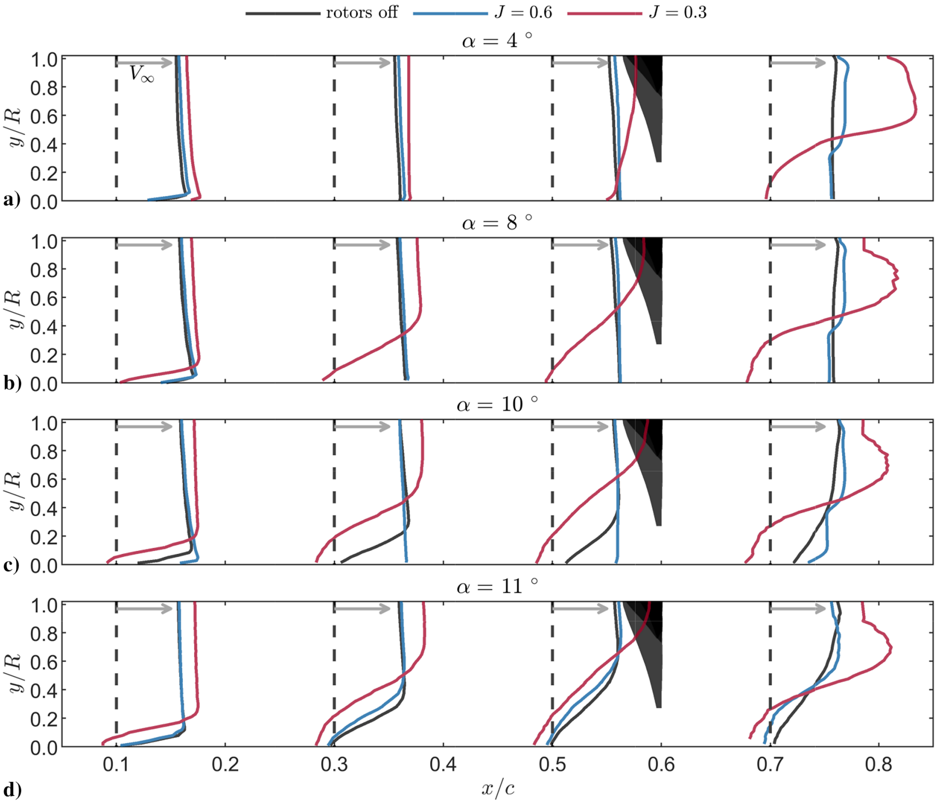

Fig. 12 **Axial velocity profiles upstream of the rotor extracted at $x/c = 0.1$, $x/c = 0.3$, $x/c = 0.5$, and $x/c = 0.7$ for a) $\alpha = 4°$, b) $\alpha = 8°$, c) $\alpha = 10°$, and d) $\alpha = 12°$. The rotor position is fixed at $x_r/c = 0.6$, and the blade is shown by the black surface. To provide an indication of the velocity magnitude of the profile, a gray arrow is shown with its length being representative of the freestream velocity magnitude.**

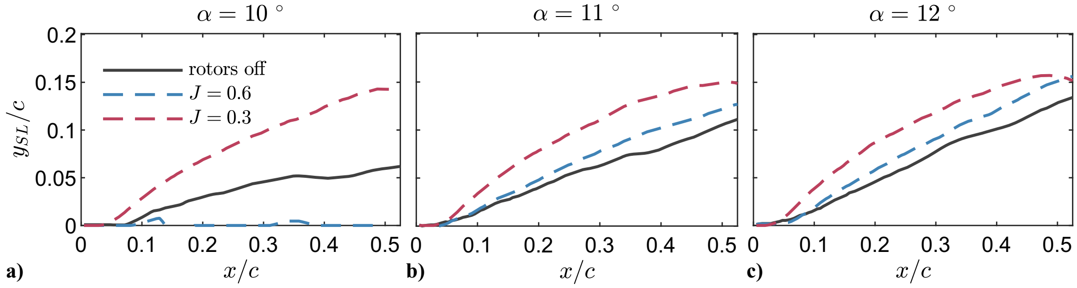

Fig. 13 **Normalized shear layer height $y_{\mathrm{SL}}/$ for a) $\alpha = 10°$, b) $\alpha = 11°$, and c) $\alpha = 12°$. The rotor position is fixed at $x_r/c = 0.6$.**

The shear layer height is identified from the velocity field as the maximum of the vertical derivative of the velocity magnitude, i.e., $y_{\mathrm{SL}} = \max(\mathrm{d}V/\mathrm{d}y)$. For the rotors-off conditions, the shear layer adheres to a rather linear profile as a function of the chordwise coordinate x, the slope of which increases with the angle of attack. With the rotors operating at $J = 0.6$, the flow is still attached for $\alpha = 10°$, as shown in Fig. 13a. For the larger values of α, the data for this advance ratio show a similar straight function of the boundary-layer thickness as the rotors-off condition, although with an increased slope (see Figs. 13b and 13c). Moreover, the separation point is unaffected by the rotors for this advance ratio. The increased suction of $J = 0.3$ generates a thicker, parabolic shape for the boundary-layer thickness, which is independent of α. Based on these experimental results, an approximate, linear function for the shear layer ingestion height is implemented in the model [recall the discussion on Eqs. (6) and (7)].

V. Model Validation

Trends in the aeropropulsive performance of the wing–rotor-array system are now described and compared between the empirical observations and the model predictions. First, we start with a validation of the modeled flow features (Sec. V.A), after which the propulsive thrust and wing lift augmentation are covered in Secs. V.B–V.C.

A. Rotor-Induced Effects

In Sec. II.C, three rotor-induced flow features were introduced that form the foundation of the lift part of the aeropropulsive model. Both the presence of the upwash ($\Delta c_{l,\alpha}$) and thrust vectoring ($\Delta c_{l,tv}$) sources of lift and their dependence on rotor positioning are validated with the experimental PIV data. Note that validation of the projected streamtube pressure ($\Delta c_{l,p}$) is excluded here, as the other rotor-induced lift-generating contributions affect the experimental wing pressure values, making direct comparison unreliable. Nonetheless, a simplified comparison, for a condition where the effects of the other lift contributions are minimized, is included in Appendix D.

Recall that the upwash is generated by the rotor contraction upstream of the wing. To validate this flow feature, the system's inflow angle is extracted from a quarter wing chord upstream of the wing and averaged over a vertical length of half a wing chord ($x/c = -0.25$, $y/c = [-0.25, 0.25]$) using the measured velocity fields. This sample domain is outside of the stagnation region of the wing, and small variations in the horizontal position gave consistent results. The change in inflow angle, $\Delta\alpha$, due to the rotors induction is taken by subtracting the rotors-off inflow angle from the value of the installed configuration.

In Fig. 14a, the generated upwash as a function of the geometric angle of attack for a rotor position of $x_r/c = 0.3$ is considered. This rotor position was chosen to eliminate the effect of the confined streamtube (recall the discussion on the correction factor C_1 in Sec. II.C.1). The results show positive values of $\Delta\alpha$, corresponding to an increase in the angle of attack by operation of the rotors. Experimental data of the low-advance ratio of $J = 0.6$, indicated by the markers, present a decreasing trend with α until reaching the stall angle of $\alpha = 12°$. After this, the value of $\Delta\alpha$ increases gradually, reaching a plateau of $\Delta\alpha \approx 5°$. The trend for $J = 0.3$, is comparable to that of $J = 0.6$, although the positive slope of $\Delta\alpha$ occurs at a lower value of α, caused by the generation of the flow reversal between rotors and wing, as was shown in Fig. 10h. The significant increase in the effective angle of attack in poststall conditions can be explained by the flow nonuniformity that is generated by the ingestion of the shear layer. Such conditions cause an abrupt increase in rotor induction in the lower half of the rotor array, and therefore more fluid is entrained around the wing's leading edge.

Predictions of $\Delta\alpha$ only concern conditions where the flow at the leading edge is attached (i.e., $\alpha \leq 10°$). As such, the modeled relations for $\Delta\alpha$ are shown with the dashed lines up to $\alpha = 10°$ and show a similar decreasing trend with α, although with an initial overestimation for $J = 0.3$.

In Fig. 14b, the increase in inflow angle $\Delta\alpha$ is shown for different chordwise rotor positions and $\alpha = 0°$. The experimental data show a constant value for $J = 0.6$ and a linear decreasing trend with rotor position for $J = 0.3$.

For $J = 0.6$, the rotor vertical position exceeds the predicted streamtube height, and no correction takes place (i.e., $C_1 = 1$ in Eqs. (12) and (13)). Nonetheless, the modeled results show a lower value of $\Delta\alpha$ for the mid- and aft-mounted rotor. Note that a rotor also induces a flow outside of the streamtube by its vortex system [26]. Such complex effects are not included in the model but could explain the discrepancies in low-thrust conditions.

Another lift contribution in the aeropropulsive model is the deflection of the rotors' slipstreams by the wing's contour (i.e., $\Delta c_{l,tv}$). This effect is validated by tracking the slipstream boundaries (localized using the extreme values of the vertical derivative of the velocity magnitude, i.e., $\mathrm{d}V/\mathrm{d}x$) and taking the average position of the top and bottom boundary. Then, the local angle of the streamtube is fitted by a linear function and extracted at $x/c = 1.1$. Finally, the streamtube angle directly behind the disk (at $x/c = x_r/c + 0.15$) is removed from this value to obtain the deflection angle ϵ. The slipstream deflection angle ϵ is presented in Fig. 14c for $\alpha = 0°$ and shows large differences between the lower and higher advance ratios. The higher advance ratio of $J = 0.6$ shows a negative ϵ, corresponding to the slipstream being deflected downward. For a lower advance ratio of $J = 0.3$, the deflection angle ϵ is positive, due to the slipstream separation (see Figs. 10g and 12a). Note that the modeled slipstream deflection is independent of the advance ratio and resembles the results for $J = 0.6$.

B. Propulsive Thrust

Results of the rotor's thrust coefficient C_T as a function of the angle of attack α are presented in Fig. 15 for the three chordwise rotor positions and $J = 0.3$ and $J = 0.6$. Here, the mean of repeated experimental results is presented by the markers, while

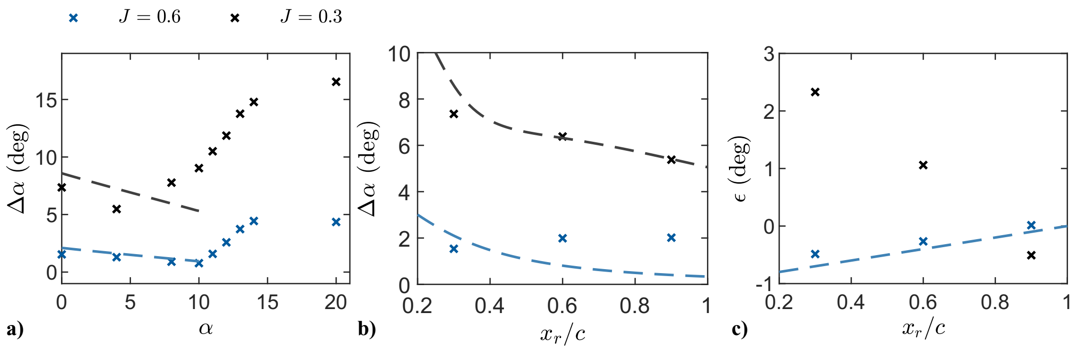

Fig. 14 Comparison between modeled (dashed lines) and measured (markers) rotor-induced flow features: a) the increase in inflow angle $\Delta\alpha$ compared to the rotors-off condition (extracted at $(x/c, y/c) = (-0.25, [-0.25, 0.25])$) for $x_r/c = 0.3$, as a function of α; b) the increase in inflow angle $\Delta\alpha$ for $\alpha = 0°$ as a function of rotor positioning; and c) the averaged angle of the rotor slipstream ϵ extracted at $x/c = 1.05$.

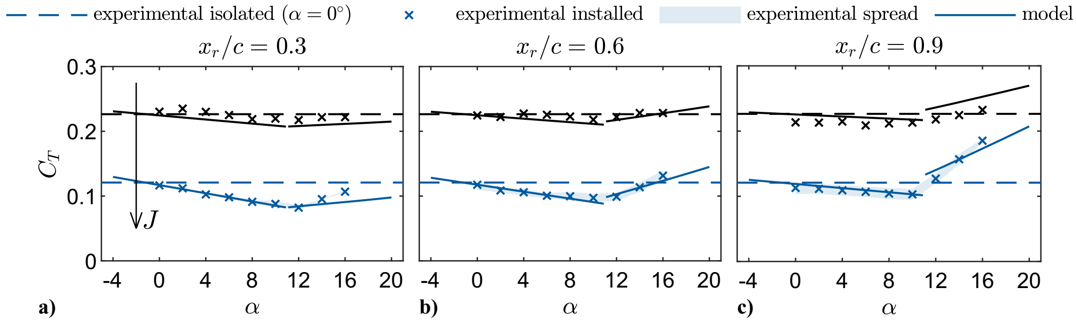

Fig. 15 **Center rotor's thrust coefficient C_T for a) $x_r/c = 0.3$, b) $x_r/c = 0.6$, and c) $x_r/c = 0.9$. Experimental results have been averaged over repeated measurements. The spread in the values of the installed configuration is shown by the translucent surfaces. The solid lines present the modeled trends. The different colors indicate different values of the advance ratio: $J = 0.3$ (black) and $J = 0.6$ (blue).**

the hatched area resembles the repeatability of independent load measurements.

For the installed configuration, the thrust is reduced with respect to the isolated rotor for most of the concerned angles of attack. Below $\alpha = 12°$, a downward trend with inclination is visible. The slope of this trend increases for a more forward-positioned rotor and with the advance ratio J. The model results, shown by the solid lines, capture these effects. This indicates that the loss in thrust can be attributed to the increasing circulation of the wing.

Around the stall angle of the wing, i.e., $\alpha = 10°$, the thrust increases again. Placing the rotor further toward the trailing edge increases the amount of re-ingestion, having a larger effect on the thrust augmentation. Since the stall criterion is a singularity in the model, this is also returned in the thrust predictions, while the measurements show a smoother pattern along stall conditions. The model slightly underpredicts the slope of the thrust in these conditions. This can be attributed to the increase in shear layer height by the operation of the rotors (recall Fig. 13). This increment in the re-ingestion region is not included in the model.

C. Wing Lift

The lift increase of the wing, by the rotor-induced flow, is presented in Fig. 16, by the lift coefficient c_l. For the predictions, the lift increase by rotor induction Δc_l is combined with the isolated wing's lift coefficient c_l (obtained through the Viterna and Corrigan model [27]).

In Fig. 16, the rotors-off condition shows the lift curve with the well-known features: a linear regime up until the stall angle of $\alpha = 12°$, after which the lift is reduced. Operation of the rotors increases the lift for each of the investigated chordwise rotor positions, advance ratios, and angles of attack. This lift enhancement decreases with the advance ratio J, as shown by the trend arrow in Fig. 16a.

In the prestall regime of the lift curve, i.e., $\alpha < 12°$, the results of the wing with rotors installed show a reduced slope compared to the rotors-off condition. This is caused by the fact that the rotor's thrust is reduced with inclination, therefore reducing the induced flow as well. Considering the chordwise position of the rotor, the aft-mounted rotor, i.e., $x_r/c = 0.9$ in Fig. 16c, shows an increase in c_l by 10% compared to the forward rotor position of $x_r/c = 0.3$. The lift enhancement compared to the rotors-off conditions is abruptly amplified once the stall angle is reached. This is ascribed to the increase in the effective angle of attack (Fig. 15).

The model predictions, for prestall conditions, show a comparable increase in lift and a similar reduction of the slope for $J = 0.3$. Nonetheless, the lift increase for the mid- and aft-positioned rotor is slightly underestimated for $J = 0.6$. For these conditions, the rotor vertical position y_r exceeds the modeled streamtube height $R_s(x')$; i.e., the wing is located outside the rotors' streamtubes, and the model predicts only a marginal lift increase. In reality, rotors induce flow outside of the streamtube region by their vortex systems [14]. Such complex vortex-induced velocities are not considered in the model but can contribute to the lift of over-the-wing propulsion in low-thrust conditions [26], explaining the observed discrepancies.

To show the variations with rotor positioning more clearly, the lift increase Δc_l as a function of the rotor position x_r/c is presented in Fig. 17 for a moderate ($\alpha = 0°$) and high angle of attack ($\alpha = 6°$). Here, the modeled contributions to the lift have been decomposed to highlight the effect of the different aerodynamic features.

In Fig. 17, the measurements show variations in lift coefficient with chordwise rotor position x_r/c of up to 10%. For moderate inclination of $\alpha = 0°$ in Fig. 17a, a maximization of the lift for a midpositioned rotor is found, while the rotor positioned closest to the leading edge gives the lowest lift enhancement. Instead, for the higher inclination (Fig. 17b), a linear behavior with rotor position is found, in which the lift for the aft-mounted rotor is 18% higher than for the forward-mounted rotor.

The predictions show an increase in lift coefficient with rotor position x_r, although a local enhancement in lift around $x_r/c = 0.3$ due to the effective angle of attack is also observed. The decomposition of the modeled components shows that the lift increase due

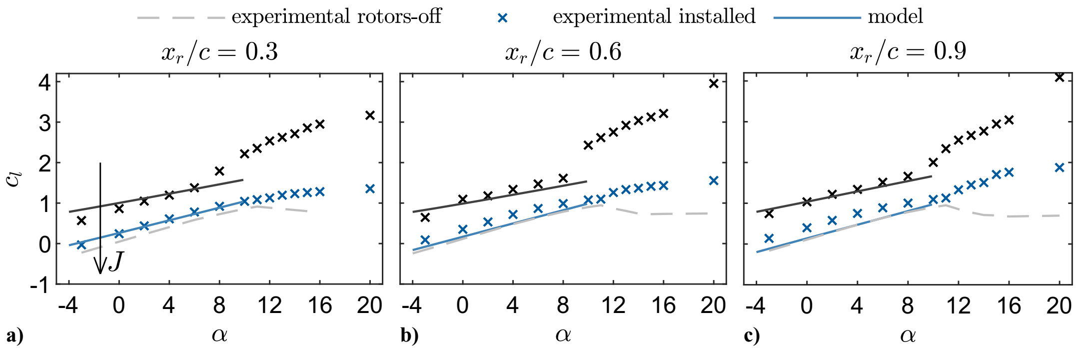

Fig. 16 **Wing's lift coefficient c_l for a) $x_r/c = 0.3$, b) $x_r/c = 0.6$, and c) $x_r/c = 0.9$. The solid lines present the modeled trends. The different colors indicate different values of the advance ratio: $J = 0.3$ (black) and $J = 0.6$ (blue). The rotors-off condition is shown by the gray line for $Re_c = 480{,}00$.**

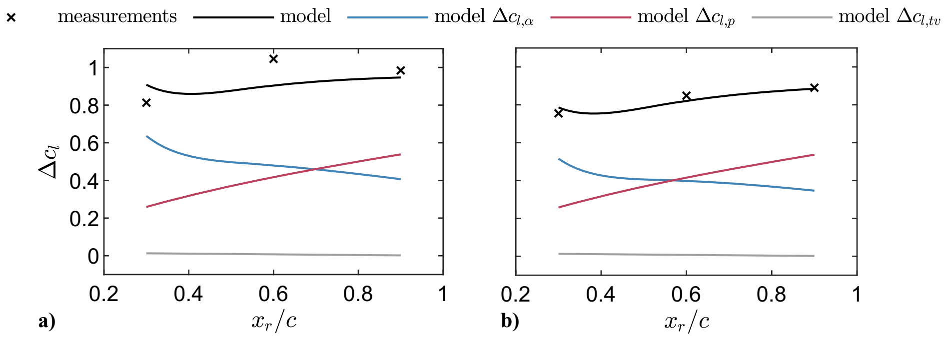

Fig. 17 Difference in lift coefficient Δc_l compared to the isolated wing and decomposition of the model components, as a function of rotor spacing, for $J = 0.3$ and a) $\alpha = 0°$ and b) $\alpha = 6°$.

to the projected pressure distribution $\Delta c_{l,p}$, and the increase in the effective angle of attack $\Delta c_{l,\alpha}$ are comparable in magnitude for a midmounted rotor. For a forward-mounted rotor, $\Delta c_{l,\alpha}$ clearly becomes the dominant term, while for the aft-mounted rotor, the lift is prevailed by the reduced pressure due to rotor suction. $\Delta c_{l,\alpha}$ is, however, more strongly reduced by inclination than $\Delta c_{l,p}$, which could explain varying trends with α observed in the experimental data. The predicted increase in lift due to streamtube deflection $\Delta c_{l,tv}$ shows to be negligible for the used airfoil, due to the limited amount of camber.

VI. Conclusions

A semi-analytical model is proposed that captures the aeropropulsive performance trends of fixed-pitch, over-the-wing rotors at incidence. The model employs a single-pass strategy resulting in an expression where the dominant performance and geometric design parameters appear explicitly. Consequently, the model bears relevance to the understanding of the aeropropulsive performance of such a system during the transition from vertical to horizontal flight. The installed rotor's thrust is modeled through the definition of an effective advance ratio, determined by the inviscid velocity increase by the wing's circulation and the predicted momentum deficit by shear layer ingestion. Model predictions and experimental data reveal a similar reduction in rotor thrust when rotors are positioned over the suction side of the wing. The difference compared to the isolated rotor depends on a combination of the advance ratio, angle of attack, and the chordwise position over the wing. In the prestall regime, the thrust is reduced most significantly for the rotor position near the wing's leading edge. Around the wing's stall angle, the rotor operated in low-thrust conditions showed to energize the boundary layer, resulting in a delay of leading-edge separation by approximately 1 deg. Increasing the thrust was shown to be unsuccessful in increasing this delay, because flow-reversal regions appeared due to the adverse pressure gradient generated by the rotors.

The rotors' induced flow affects the wing's lift through a generated upwash, the projection of the streamtube pressure on the wing's surface, and the deflection of the streamtube. In the prestall regime, these effects increase lift but reduce the lift slope compared to the rotors-off conditions. The reduced slope is the result of the reduction of thrust by the increasing circulation provided by the wing and the decreasing contribution of the rotor-induced upwash with geometric inclination. For most of the investigated parameter space, the aft-mounted rotor showed the highest value of the lift, up to 10% higher than the forward-mounted rotor. The model predicts the general trends of the lift curve, but discrepancies are found for the low thrust conditions. These are expected to stem from the induced velocity outside the streamtube region, generated by the rotor vortex system, which is not considered in the model. On that note, the complex, viscous interactions due to the streamtube–wing adherence downstream of the rotors are not included in the model but could affect the pressure and thrust vectoring terms of the lift prediction. Such effects could be included through empirical relations to correct the model results.

Although the effect of the rotors on the leading edge separation is marginal, an abrupt increase in lift was observed once separation occurred. This is the result of an additional increase in the rotor-induced upwash while maintaining the separation point at the same position along the wing's chord as for the rotors-off condition.

Appendix A: Derivation of the Thrust Model

A.1. Circulation

The induced velocity by circulation is approached by the integration of the bound vorticity of the wing. The wing's circulation Γ_{tot} based on the lift coefficient c_l reads

$$\Gamma_{\text{tot}} = \frac{c_l V_\infty c}{2} \tag{A1}$$

It is assumed that the circulation Γ_{tot} forms a parabolic distribution along the wing's chord, from which the circulation distribution $\Gamma(x)$ follows:

$$\Gamma(x) = \frac{3}{2}\left(1 - \left(\frac{x}{c}\right)^2\right)\Gamma_{\text{tot}} = \frac{3}{4} c_l V_\infty c \left(1 - \left(\frac{x}{c}\right)^2\right) \tag{A2}$$

The induced velocity by the two-dimensional bound circulation distribution is then computed by the integration of Biot–Savart law. For the horizontal induced velocity $V_{\Gamma,x}$ at a rotor position (x_r, y_r) this reads:

$$\begin{aligned}\frac{V_{\Gamma,x}}{V_\infty} &= -\frac{1}{2\pi V_\infty}\int_0^s \frac{\Gamma(x)\left(\frac{y_r}{c} - \frac{y_\gamma(s)}{c}\right)}{\left(\frac{x_r}{c} - \frac{x_\gamma(s)}{c}\right)^2 + \left(\frac{y_r}{c} - \frac{y_\gamma(s)}{c}\right)^2}\,\mathrm{d}s \\ &= -\frac{c}{2\pi V_\infty}\int_0^1 \frac{\gamma(x) y_r}{(x_r - x_\gamma)^2 + y_r^2}\,\mathrm{d}x_\gamma \end{aligned} \tag{A3}$$

in which s is defined as the line of the vorticity distribution, given by the x- and y-coordinates x_γ and y_γ, respectively. The vorticity source is considered as a horizontal line (i.e., $y_\gamma 0$), which returns the right-hand side of Eq. (A3). Then, by substitution of Eq. (A2) in Eq. (A3) and working out the integral, the final expression for the normalized axial induced velocity yields:

$$\begin{aligned}\frac{V_{\Gamma,x}}{V_\infty} = \frac{3c_l}{8\pi c^2}\Bigg(& x_r y_r \ln\left(\frac{x_r^2 + y_r^2}{(c - x_r)^2 + y_r^2}\right) \\ &+ (x_r^2 - y_r^2 - c^2)\left(\tan^{-1}\left(\frac{x_r - c}{y_r}\right) - \tan^{-1}\left(\frac{x_r}{y_r}\right)\right) - y_r c\Bigg)\end{aligned} \tag{A4}$$

A.2. Shear Layer Ingestion

At sufficiently large angles of attack, the wing's boundary layer will separate from the wing. The correction for the effect is given by J_{SL}:

$$J_{\mathrm{SL}} = 1 - f(\alpha, \alpha_c)\left(1 - \frac{V_{\mathrm{SL}}}{V_\infty}\right)\frac{A_{\mathrm{SL}}}{\pi R_1^2} \tag{A5}$$

For simplicity, the velocity below the shear layer is assumed to be zero, i.e., $V_{\mathrm{SL}} = 0$. The function $f(\alpha, \alpha_c)$ in Eq. (A5) is a stall criterion which has the form of

$$f(\alpha, \alpha_c) = \frac{(\alpha - \alpha_c)}{2\sqrt{((\alpha - \alpha_c))^2}} + \frac{1}{2}, \quad \alpha_c = 0.818\sqrt{\frac{r}{c}} \tag{A6}$$

The area A_{SL}, can then be found by integrating the rotor disk area below the shear layer height:

$$A_{\mathrm{SL}} = \int_{y_r - R_1}^{y_{\mathrm{SL}}} \sqrt{(y - y_r)^2 + R_1^2}\,\mathrm{d}y \tag{A7}$$

in which $y_{\mathrm{SL}}(x)$ corresponds to the shear layer height of the installed wing, at the chordwise position of the rotor x_r:

$$y_{\mathrm{SL}}(x) = \left(\frac{11}{8}\right)x_r \tan(\alpha) \tag{A8}$$

Integration of Eq. (A7) and substitution in Eq. (A5) leads to the exact expression of J_{SL}:

$$\begin{aligned} J_{\mathrm{SL}} = 1 - \left(\frac{(\alpha - \alpha_c)}{2\sqrt{((\alpha - \alpha_c))^2}} + \frac{1}{2}\right)\Bigg(&\frac{y_{\mathrm{SL}}(x) - y_r}{\pi R_1^2}\sqrt{R_1^2 - (y_{\mathrm{SL}}(x) - y_r)^2} \\ &+ \frac{1}{\pi}\tan^{-1}\left(\frac{y_{\mathrm{SL}}(x) - y_r}{\sqrt{R_1^2 - (y_{\mathrm{SL}}(x) - y_r)^2}}\right) + \frac{1}{2}\Bigg) \end{aligned} \tag{A9}$$

Appendix B: Derivation of the Lift Model

B.1. Streamtube Properties

Using the approach of Veldhuis [14], the rotor disks are modeled as uniform distributions of pressure doublets with strength $\Delta p = p_2 - p_1$. Here, p_1 indicates the pressure in a point directly in front and p_2 directly after the rotor disk. Considering a reference point r at a given distance l_r from the rotor disk, the pressure in r is found by:

$$p_r = \frac{\Delta p}{4\pi}\int_S \frac{\partial}{\partial n}\left(\frac{1}{l_r}\right)\mathrm{d}S \quad \text{for } l_r > 0 \tag{B1}$$

in which S is the surface of the distribution of pressure doublets. Rather than a circular disk, the rotor array is modeled by a rectangular surface with length $2N_R R_1$ and width $2R_1$. Considering a reference point in the center of the streamtube (i.e., $y = 0$, $z = 0$, and $n = x$), the pressure returns:

$$p_r = \frac{\Delta p}{4\pi}\int_{N_r R_1}^{N_r R_1}\int_{-R_1}^{R_1} -\frac{x}{(x^2 + y_1^2 + z_1^2)^{3/2}}\,\mathrm{d}y_1\,\mathrm{d}z_1 \tag{B2}$$

Solving the integral of Eq. (B2) returns the streamwise distribution of pressure $p(x)$ for a rectangular streamtube:

$$p(x) = \frac{\Delta p}{\pi}\tan^{-1}\left(\frac{N_r R_1^2}{x\sqrt{(N_r^2 + 1)R_1^2 + x^2}}\right) \tag{B3}$$

The axial-induced velocity $v_a(x)$ upstream and downstream of the disk then follows directly from the result Eq. (B3) and the momentum equation [14]:

$$\frac{v_a(x)}{V_\infty} = a\left(\frac{x}{\sqrt{x^2}} + 1 - \frac{2}{\pi}\tan^{-1}\left(\frac{N_r R_1^2}{x\sqrt{(N_r^2 + 1)R_1^2 + x^2}}\right)\right) \tag{B4}$$

in which

$$a = \frac{\Delta p}{2\rho V_\infty^2} \tag{B5}$$

Considering $N_r = 5$, the term within brackets in Eqs. (B3) and (B4) reduces to

$$\frac{N_r R_1^2}{x\sqrt{(N_r^2 + 1)R_1^2 + x^2}} \approx \frac{R_1}{x} \quad \text{for } N_r \geq 5 \tag{B6}$$

Consequently, the streamwise distribution of pressure $p(x)$ and induced velocity $v_a(x)$ approaches the two-dimensional solution:

$$\begin{aligned} p(x) &= \frac{\Delta p}{\pi}\tan^{-1}\left(\frac{R_1}{x}\right) \\ \frac{v_a(x)}{V_\infty} &= a\left(\frac{x}{\sqrt{x^2}} + 1 - \frac{2}{\pi}\tan^{-1}\left(\frac{R_1}{x}\right)\right) \end{aligned} \tag{B7}$$

Finally, by the continuity equation and the result of Eq. (B7), the height of the two-dimensional streamtube $R_s(x)$ yields:

$$\frac{R_s(x)}{R_1} = \frac{1 + a}{1 + a\left(\frac{x}{\sqrt{x^2}} + 1 - \frac{2}{\pi}\tan^{-1}\left(\frac{R_1}{x}\right)\right)} \tag{B8}$$

B.2. Effective Angle of Attack

The increase in lift by the effective angle of attack $\Delta c_{l,\alpha}$ follows from the difference between the predicted installed and the isolated wing's inflow angle $\Delta\alpha$:

$$\Delta c_{l,\alpha} = \overbrace{2\pi}^{\substack{\text{lift}\\ \text{slope}}}\ \overbrace{\Delta\alpha}^{\substack{\text{increase}\\ \text{angle of}\\ \text{attack}}}\ \overbrace{\frac{2N_r R_1}{S}}^{\substack{\text{affected}\\ \text{span}}} = 2\pi\cos^{-1}\left(\frac{\boldsymbol{a}\cdot\boldsymbol{b}}{|\boldsymbol{a}||\boldsymbol{b}|}\right)\frac{2N_r R_1}{S} \tag{B9}$$

in which the term on the right side corrects the result for the affected span region of the wing. The two-dimensional velocity vectors ***a*** and ***b*** are for the installed configuration and isolated wing respectively, at the wing's leading edge:

$$\mathbf{a} = \begin{bmatrix} \dfrac{v_a(-x_r)}{V_\infty} + \cos(\alpha) \\ \dfrac{v_i(-x_r)}{V_\infty} + \sin(\alpha) \end{bmatrix}, \quad \mathbf{b} = \begin{bmatrix} \cos(\alpha) \\ \sin(\alpha) \end{bmatrix} \tag{B10}$$

Substitution of Eq. (B10) in Eq. (B9), applying the small-angle approximation for α, gives the expression for $\Delta\alpha$:

$$\Delta\alpha = \cos^{-1}\left(\frac{\left(1 - \dfrac{\alpha^2}{2}\right)\dfrac{v_a(-x_r)}{V_\infty} + \alpha\dfrac{v_i(-x_r)}{V_\infty} + 1}{\sqrt{\left(\dfrac{v_a(-x_r)}{V_\infty} + 1 - \dfrac{\alpha^2}{2}\right)^2 + \left(\dfrac{v_i(-x_r)}{V_\infty} + \alpha\right)^2}}\right) \tag{B11}$$

The axial induced velocity v_a upstream of the disks follows from Eq. (B7), resulting in:

$$\frac{v_a(x)}{V_\infty} = -\frac{2a}{\pi}\tan^{-1}\left(\frac{R_1}{x}\right) \quad \text{for } x < 0 \tag{B12}$$

By the acceleration in the axial direction, the flow will be entrained from the vertical direction by a velocity v_i, which follows from the law of continuity:

$$\frac{v_i(x)}{V_\infty} = C_1 \frac{\mathrm{d}\left(\dfrac{v_a(x)}{V_\infty}\right)}{\mathrm{d}x} R_1 = C_1 \frac{2aV_\infty R_1^2}{\pi(x^2 + R_1^2)} \quad \text{for } x < 0 \tag{B13}$$

In Eq. (B13) the coefficient C_1 is used to correct the results for the blockage of the wing, limiting the contraction of the streamtube in high thrust conditions (recall Fig. 7). This results in a higher axial velocity and lower static pressure upstream of the disk than the predictions of Eq. (B7), which concern a free contraction of the streamtube. Consequently, this effect is expected to generate a greater upwash at the wing's leading edge, and scales with the overlap between the free-contraction stream tube height R_s and the vertical rotor position y_r:

$$C_1 = f\left(\frac{R_s(-x_r) - y_r}{R_1}\right) \approx c_0\left(\frac{R_s(-x_r) - y_r}{R_1}\right)^{c_1} + 1 \tag{B14}$$

A power function is then formed using the expression of the overlap region, as shown on the right side of Eq. (B14). The final expression for C_1 is found by minimization of the L_2-norm between the predicted and measured upwash (as used to generate Figs. 14a and 14b). During the minimization, only integer values for c_0 are considered, while c_1 uses both integers and half-integers:

$$C_1 = \max\left(1, 60\left(\frac{R_s(-x_r) - y_r}{R_1}\right)^{5/2} + 1\right) \tag{B15}$$

B.3. Streamtube Pressure

The effect of the projected streamtube pressure is only considered when the maximum streamtube height R_s exceeds the vertical rotor spacing y_r. The effect of this pressure on the lift of the wing $\Delta c_{l,p}$ is computed through:

$$\Delta c_{l,p} = \overbrace{\frac{2N_rR_1}{S}}^{\text{affected span}} \overbrace{\frac{2}{\rho V_\infty^2 c}}^{\text{lift normalization}} \int_{-x_r}^{c-x_r} p^*(x')\,\mathrm{d}x', \quad \text{for } \frac{\lim_{x'\to-\infty} R_s(x')}{y_r} = \frac{R_1(a+1)}{y_r} > 1 \tag{B16}$$

in which $p^*(x')$ is the projected streamtube pressure over the wing surface. This pressure is based on the relation for the streamtube pressure $p(x')$ [Eq. (B7)] and includes a correction due to the effect of the streamtube confinement (recall Fig. 7). The streamtube confinement leads to a reduction in effective streamtube height, leading to an increase in axial velocity. $g(x', y_r)$ corrects the axial velocity to find v^*:

$$v^*(x') = (v_a(x') + V_\infty)g(x', y_r) = (v_a(x') + V_\infty)\frac{R_s(x')}{y_r}, \quad \text{for } \frac{R_s(x')}{y_r} > 1 \tag{B17}$$

The correction function $g(x', y_r)$ is defined as the ratio between the free-contraction $R_s(x')$ and confined contraction streamtube height y_r. Using Bernoulli's equation, the pressure $p^*(x')$ yields the free-contraction stream tube pressure [Eq. (B7)] and a second term that includes the streamtube confinement effect:

$$p^*(x') + \frac{\rho}{2}(v_a(x') + V_\infty)^2 g(x', y_r)^2 = p(x') + \frac{\rho}{2}(v_a(x') + V_\infty)^2 \tag{B18}$$

$$p^*(x') = p(x') - \frac{\rho}{2}(v_a(x') + V_\infty)^2(1 - g(x', y_r)^2) \tag{B19}$$

Equation (B19) is then integrated during which the integrals are split, and only the upstream part of the rotor's streamtube is considered:

$$\int_{-x_r}^{c-x_r} p^*(x')\,\mathrm{d}x' \approx \int_{-x_r}^{0} p(x') - \int_{-x_r}^{0} \frac{\rho}{2}(v_a(x') + V_\infty)^2(1 - g(x', y_r)^2)\,\mathrm{d}x' \tag{B20}$$

The first term of Eq. (B20) is found by integrating Eq. (B7):

$$\int_{-x_r}^{0} p(x')\,\mathrm{d}x' = \frac{\Delta p}{\pi}\left(\frac{1}{2}R_1 \ln\left(\frac{R_1^2}{R_1^2 + x_r^2}\right) + x_r \tan^{-1}\left(\frac{R_1}{-x_r}\right)\right) \tag{B21}$$

The second term of Eq. (B20) is further simplified by defining the axial velocity and rotor contraction as the averaged value of the freestream condition and the rotor disk:

$$v_a(x') + V_\infty \approx \frac{\lim_{x'\to-\infty} v_a(x') + v_a(0)}{2} + V_\infty = V_\infty\left(\frac{a}{2} + 1\right) \tag{B22}$$

$$R_s(x') \approx \frac{\lim_{x'\to-\infty} R_s(x') + R_s(0)}{2} = R_1\left(\frac{a}{2} + 1\right) \tag{B23}$$

This reduces the second term of Eq. (B20) to:

$$\begin{aligned} &-\int_{-x_r}^{0} \frac{\rho}{2}(v_a(x') + V_\infty)^2(1 - g(x', y_r)^2)\,\mathrm{d}x' \\ &\approx -\int_{-x_r}^{0} \frac{\rho V_\infty^2}{2}\left(\frac{a}{2} + 1\right)^2\left(1 - \left(\frac{R_1}{y_r}\left(\frac{a}{2} + 1\right)\right)^2\right)\mathrm{d}x' \\ &\approx \frac{x_r \rho V_\infty^2}{2}\left(\frac{a}{2} + 1\right)^2\left(1 - \left(\frac{R_1}{y_r}\left(\frac{a}{2} + 1\right)\right)^2\right) \end{aligned} \tag{B24}$$

Substituting Eqs. (B20) and (B21) in Eqs. (B24) and (B16) gives the final expression of $\Delta c_{l,p}$:

$$\begin{aligned} \Delta c_{l,p} = \frac{2N_rR_1}{Sc}\Bigg(&\frac{4a}{\pi}\left(\frac{1}{2}R_1 \ln\left(\frac{R_1^2}{R_1^2 + x_r^2}\right) + x_r \tan^{-1}\left(\frac{R_1}{-x_r}\right)\right) \\ &+ x_r\left(\frac{a}{2} + 1\right)^2\left(1 - \left(\frac{R_1}{y_r}\left(\frac{a}{2} + 1\right)\right)^2\right)\Bigg) \end{aligned} \tag{B25}$$

B.4. Thrust Vectoring

From a momentum balance, the lift increase due to a stream tube deflection by ϵ yields:

$$\Delta c_{l,tv} = \frac{2S_e(V_e - V_\infty)^2 \sin(\epsilon)}{V_\infty^2 c} \tag{B26}$$

In the aeropropulsive model, the angle ϵ is based on the flow deflection by the isolated wing ϵ_w under $\alpha = 0°$, and it is assumed that this depends linearly on the position of rotor along the wing's chord:

$$\varepsilon = \epsilon_w\left(1 - \frac{x_r}{c}\right) = \frac{2c_{l,0}c}{\pi S}\left(1 - \frac{x_r}{c}\right) \tag{B27}$$

The streamtube cross-sectional surface S_e and velocity V_e are extracted by taking the limit of the streamtube contraction R_s and velocity V_a:

$$S_e = 2N_r R_1 \lim_{x' \to \infty} (2R_s(x')) = 4N_r R_1^2 \frac{1+a}{1+2a} \tag{B28}$$

$$V_e = \lim_{x' \to \infty} (V_a(x')) + V_\infty = (2a+1)V_\infty \tag{B29}$$

Substitution of Eq. (B27), Eq. (B28) and Eq. (B29) in Eq. (B26) and assuming small angles for ϵ, results in the final expression of the lift increase by slipstream deflection $\Delta c_{l,tv}$:

$$\Delta c_{l,tv} = \frac{64 N_r R_1^2 (1+a) a^2 c_{l,0}}{(1+2a)\pi S} \left(1 - \frac{x_r}{c}\right) \tag{B30}$$

Appendix C: Validation of the Single-Pass Strategy

The mutual interference of rotors and wing has been modeled using a single-pass strategy. To validate this approximation, predictions are compared to results obtained from running the same model over multiple iterations. These iterations are performed by including the rotor-induced lift [Eq. (10)] in the circulation distribution of the wing [Eq. (4)] and recomputing the effective advance ratio [Eq. (2)]. The found thrust C_T and lift coefficient c_l for different iterations i, normalized by the single-pass results, are presented in Fig. C1.

The results presented in Fig. C1 correspond to the rotor position that exhibited the greatest deviation between the single-pass (iteration 1) and the converged results, within the investigated parameter space. Both thrust and lift values converge after the third iteration and show a reduction compared with the single-pass results of up to 5%, dependent on the advance ratio.

Appendix D: Validation of Projected Streamtube

Validation of the projected streamtube mechanism $\Delta c_{l,p}$ is performed by comparison with the experimental pressure distribution below the rotor axis. It is important to note that other rotor-induced lift-generating contributions also impact the experimental pressure values of the wing (effective angle of attack, thrust vectoring). To minimize these effects, the validation is based on data for the aft-positioned rotor, without inclination ($x_r/c = 0.9$ and $\alpha = 0°$). Figure D1 displays the experimental and modeled [by Eq. (15)] rotor-induced pressure distribution for $J = 0.3$ and $J = 0.6$.

For $J = 0.3$ in Fig. D1a, a good match is observed between the experimental and modeled pressure distributions. However, discrepancies are noted near the leading edge due to the rotor-induced increase in the angle of attack in the experimental results. Furthermore, closer to the rotor ($0.6 < x/c < 0.9$) the model does not capture any rotor-induced pressure reduction because the rotor height exceeds the streamtube height, i.e., $R_s(x')/y_r < 1$. This limitation also applies to $J = 0.6$ in Fig. D1b, where the modeled rotor-induced pressure distribution equals zero, leading to an underprediction compared to the experimental value. This discrepancy is tied to the induced velocities of the rotors' vortex systems, which are not considered in the model.

Acknowledgments

This research is funded by the European Union's Horizon 2020 research and innovation program, under grant agreement no. 860103, project Enabling Optimized Disruptive Airframe–Propulsion Integration Concepts (ENODISE). The authors would like to acknowledge Tim Deleij and Laurens de Haan for their assistance during the experiments and Tom Lanters for the design of the rotor mounting.

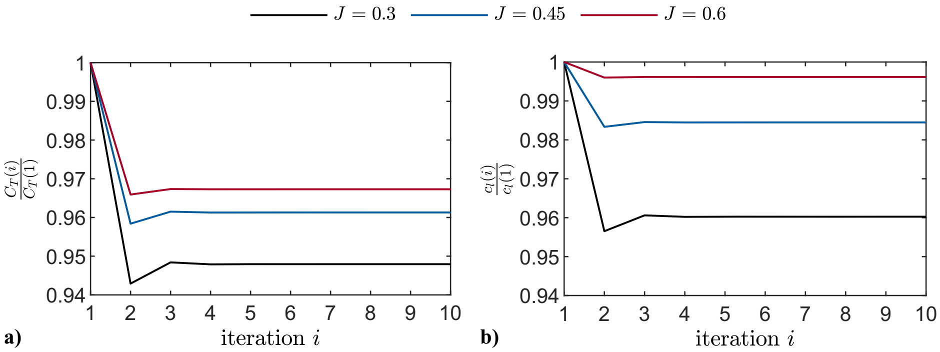

Fig. C1 **Predicted a) thrust and b) lift coefficient for different iteration numbers, normalized by the single-pass results ($i = 1$), for $x_r/c = 0.3$, $y_r/R_1 = 0.27$, and $\alpha = 8°$.**

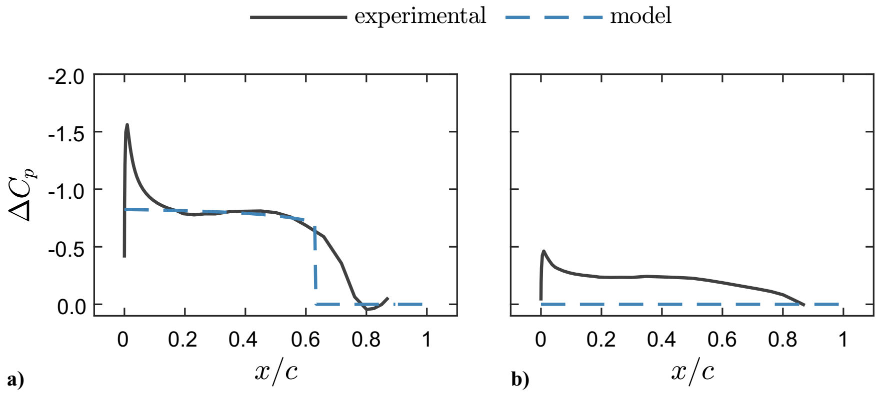

Fig. D1 **Predicted rotor-induced pressure distribution ($\Delta C_p = C_p - C_{p,\text{wing}}$) over the suction side for $x_r/c = 0.9$, $y_r/R_1 = 0.27$, and $\alpha = 0°$: a) $J = 0.3$ and b) $J = 0.6$.**

References

[1] Borer, N. K., Patterson, M. D., Viken, J. K., Moore, M. D., Bevirt, J., Stoll, A. M., and Gibson, A. R., "Design and Performance of the NASA SCEPTOR Distributed Electric Propulsion Flight Demonstrator," *16th AIAA Aviation Technology, Integration, and Operations Conference*, AIAA Paper 2016-3920, 2016. https://doi.org/10.2514/6.2016-3920

[2] Goyal, R., Reiche, C., Fernando, C., Serrao, J., Kimmel, S., Cohen, A., and Shaheen, S., "Urban Air Mobility (UAM) Market Study," NASA HQ-E-DAA-TN63717, 2018, https://ntrs.nasa.gov/citations/20190001472.

[3] Fredericks, W. J., McSwain, R. G., Beaton, B. F., Klassman, D. W., and Theodore, C. R., "Greased Lightning (GL-10) Flight Testing Campaign," NASA L-20737, 2017, https://ntrs.nasa.gov/citations/20170007194.

[4] Johnson, W., Silva, C., and Solis, E., "Concept Vehicles for VTOL Air Taxi Operations," *AHS Specialists Conference on Aeromechanics Design for Transformative Vertical Flight*, ARC–E–DAA–TN50731, 2018.

[5] Chauhan, S. S., and Martins, J. R. R. A., "Tilt-Wing eVTOL Takeoff Trajectory Optimization," *Journal of Aircraft*, Vol. 57, No. 1, 2020, pp. 93–112. https://doi.org/10.2514/1.C035476

[6] Wick, A. T., Hooker, J. R., and Zeune, C. H., "Integrated Aerodynamic Benefits of Distributed Propulsion," *53rd AIAA Aerospace Sciences Meeting*, AIAA Paper 2015-1500, 2015. https://doi.org/10.2514/6.2015-1500.

[7] Lee, T., Ni, T., and Lin, G., "Aerodynamics and Flowfield of Distributed Electric Propulsion Tiltwing During Transition with Deflected Trailing-Edge Flap," *Journal of Fluids Engineering*, Vol. 146, No. 5, 2024. https://doi.org/10.1115/1.4063934

[8] de Vries, R., and Vos, R., "Aerodynamic Performance Benefits of Over-the-Wing Distributed Propulsion for Hybrid-Electric Transport Aircraft," *Journal of Aircraft*, Vol. 60, No. 4, 2023, pp. 1201–1218. https://doi.org/10.2514/1.C036909

[9] Broadbent, E., "Noise Shielding for Aircraft," *Progress in Aerospace Sciences*, Vol. 17, 1976, pp. 231–268. https://doi.org/10.1016/0376-0421(76)90009-9

[10] Müller, L., Heinze, W., Kožulović, D., Hepperle, M., and Radespiel, R., "Aerodynamic Installation Effects of an Over-the-Wing Propeller on a High-Lift Configuration," *Journal of Aircraft*, Vol. 51, No. 1, 2014, pp. 249–258. https://doi.org/10.2514/1.C032307

[11] Perry, A. T., Bretl, T., and Ansell, P. J., "Aeropropulsive Coupling Effects on a General-Aviation Aircraft with Distributed Electric Propulsion," *Journal of Aircraft*, Vol. 58, No. 6, 2021, pp. 1351–1363. https://doi.org/10.2514/1.C036048

[12] Marcus, E. A., de Vries, R., Kulkarni, A. R., and Veldhuis, L. L., "Aerodynamic Investigation of an Over-the-Wing Propeller for Distributed Propulsion," *2018 AIAA Aerospace Sciences Meeting*, AIAA Paper 2018-2053, 2018. https://doi.org/10.2514/6.2018-2053

[13] Cooper, R., McCann, W. J., and Chapleo, A. Q., "Over Wing Propeller Aerodynamics," *ICAS Proceedings*, AIAA, Reston, VA, 1992, pp. 266–266.

[14] Veldhuis, L., "Propeller Wing Aerodynamic Interference," Ph.D. Thesis, Delft Univ. of Technology, 2005.

[15] Johnson, J. L., and White, R. E., "Exploratory Low-Speed Wind-Tunnel Investigation of Advanced Commuter Configurations Including an Over-the-Wing Propeller Design," *Aircraft Design, Systems and Technology Meeting*, AIAA Paper 1983-2531, 1983. https://doi.org/10.2514/MASTM83

[16] de Vries, R., van Arnhem, N., Avallone, F., Ragni, D., Vos, R., Eitelberg, G., and Veldhuis, L. L. M., "Experimental Investigation of Over-the-Wing Propeller–Boundary-Layer Interaction," *AIAA Journal*, Vol. 59, No. 6, 2021, pp. 2169–2182. https://doi.org/10.2514/1.J059770

[17] Cho, J., and Cho, J., "Quasi-Steady Aerodynamic Analysis of Propeller–wing Interaction," *International Journal for Numerical Methods in Fluids*, Vol. 30, No. 8, 1999, pp. 1027–1042. https://doi.org/10.1002/(SICI)1097-0363(19990830)30:8<1027::AID-FLD878>3.0.CO;2-R

[18] Marretta, R. A., Davi, G., Lombardi, G., and Milazzo, A., "Hybrid Numerical Technique for Evaluating Wing Aerodynamic Loading with Propeller Interference," *Computers & Fluids*, Vol. 28, No. 8, 1999, pp. 923–950. https://doi.org/10.1016/S0045-7930(98)00055-3

[19] Li, Z., Maltsev, V., Modarres Aval, A. H., and Da Ronch, A., "Multi-Fidelity Aerodynamic Methods for the Analysis of Propeller Wing Interaction," AIAA Paper 2024-3521, 2024. https://doi.org/10.2514/6.2024-3521

[20] Murray, H. H., Devenport, W. J., Alexander, W. N., Glegg, S. A. L., and Wisda, D., "Aeroacoustics of a Rotor Ingesting a Planar Boundary Layer at High Thrust," *Journal of Fluid Mechanics*, Vol. 850, 2018, pp. 212–245. https://doi.org/10.1017/jfm.2018.438

[21] Cerny, M., and Breitsamter, C., "Investigation of Small-Scale Propellers Under Non-Axial Inflow Conditions," *Aerospace Science and Technology*, Vol. 106, 2020, Paper 106048. https://doi.org/10.1016/j.ast.2020.106048

[22] Sinnige, T., "Aerodynamic and Aeroacoustic Interaction Effects for Tip-Mounted Propellers: An Experimental Study," Ph.D. Thesis, Delft Univ. of Technology, 2018.

[23] Okulov, V. L., Sørensen, J. N., and Wood, D. H., "The Rotor Theories by Professor Joukowsky: Vortex Theories," *Progress in Aerospace Sciences*, Vol. 73, 2015, pp. 19–46. https://doi.org/10.1016/j.paerosci.2014.10.002

[24] Tuck, E. O., "A Criterion for Leading-Edge Separation," *Journal of Fluid Mechanics*, Vol. 222, No. 1, 1991, p. 33. https://doi.org/10.1017/S0022112091000988

[25] Grande, E., Romani, G., Ragni, D., Avallone, F., and Casalino, D., "Aeroacoustic Investigation of a Propeller Operating at Low Reynolds Numbers," *AIAA Journal*, Vol. 60, No. 2, 2022, pp. 860–871. https://doi.org/10.2514/1.J060611

[26] de Vries, R., "Hybrid-Electric Aircraft with Over-the-Wing Distributed Propulsion: Aerodynamic Performance and Conceptual Design," Ph.D. Thesis, Delft Univ. of Technology, 2022.

[27] Viterna, L. A., and Corrigan, R. D., "Fixed Pitch Rotor Performance of Large Horizontal Axis Wind Turbines," *Large Horizontal-Axis Wind Turbines (NASA-CP-2230)*, NASA Conference Publication, Jan. 1982, pp. 69–86.

A. Jones
Associate Editor